Computers and Geotechnics 181 (2025) 107139

Contents lists available at ScienceDirect

Computers and Geotechnics

journal homepage: www.elsevier.com/locate/compgeo

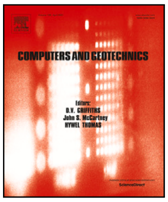

Research paper

A unified transport-velocity formulation for SPH simulation of cohesive granular materials

Shuaihao Zhang [a], Feng Wang [b], Xiangyu Hu [b], Sérgio D.N. Lourenço [a],*

[a] Department of Civil Engineering, The University of Hong Kong, Pokfulam, Hong Kong Special Administrative Region of China
[b] School of Engineering and Design, Technical University of Munich, 85748 Garching, Germany

ARTICLE INFO

Keywords:
Smoothed particle hydrodynamics
Tensile instability
Transport-velocity formulation
Cohesive granular materials
Granular flows

ABSTRACT

When simulating cohesive granular materials using smoothed particle hydrodynamics (SPH), tensile instability often arises, characterized by particle clustering and non-physical fractures. In two-dimensional scenarios, this issue is typically addressed by the artificial stress method, which introduces repulsive forces between particle pairs. However, extending this approach to three dimensions is considered complex due to the requirements of matrix diagonalization and coordinate system rotation. In this study, we introduce the transport-velocity formulation (TVF), a numerical technique widely used in SPH simulation of fluids to remove tensile instability, to address this issue. Furthermore, rather than being limited to inner particles alone as in the previous TVF, we develop a unified transport-velocity formulation (UTVF) that encompasses both free-surface and inner particles, by applying corrections to surface particles only in the tangential direction. This unified approach is tailored for large deformation and failure flow problems in cohesive granular materials, which often involve free surfaces. The proposed approach is first validated through benchmark cases of both fluids and elastic materials with known analytical solutions, demonstrating its convergence, stability, and accuracy. Comparisons with the artificial stress and particle shifting methods highlight the advantages of the UTVF in terms of momentum conservation and low dissipation. Subsequently, the developed UTVF is applied to the simulation of cohesive granular material failure and flows in both two-dimensional and three-dimensional settings. The results indicate that the proposed method effectively eliminates tensile instability, regardless of dimensionality. An open-source code is provided for further comparison and in-depth study.

1. Introduction

As a mesh-free method well-suited for simulating large material deformations, smoothed particle hydrodynamics (SPH) (Gingold and Monaghan, 1977; Lucy, 1977) has been widely applied to granular material simulations (Zhan et al., 2019; Bui and Nguyen, 2021; del Castillo et al., 2024) since its introduction by Bui et al. (2008). Over the past decade, SPH has undergone significant development, achieving notable advancements across various aspects of granular material modeling (Peng et al., 2017; Feng et al., 2022; Hoang et al., 2024). However, simulations using SPH often encounter numerical instabilities, among which tensile instability (Swegle et al., 1995; Monaghan, 2000; Gray et al., 2001)—manifested as particle clustering and non-physical fractures—is a particularly prominent issue.

In the SPH simulation of non-cohesive granular materials, tensile instability should theoretically not occur, as it arises only in tensile regions, and non-cohesive materials cannot sustain tensile forces. However, due to numerical errors in the computation (Bui et al., 2008), some particles may exhibit a hydrostatic stress component (negative for compression) greater than zero, indicating the presence of tensile forces. This numerical artifact can, in turn, result in particle clustering akin to tensile instability. To address this issue, a tension cracking treatment (Chen and Mizuno, 1990; Bui et al., 2008) is commonly employed, where the hydrostatic stress component of a particle is adjusted to zero whenever it becomes positive. This adjustment eliminates tensile forces that should not arise in non-cohesive materials, thereby mitigating the numerical instabilities caused by such forces.

When simulating cohesive granular materials, the presence of cohesion allows the material to resist tensile forces, making tensile instability more pronounced. A commonly used solution is to introduce an artificial stress term (Gray et al., 2001) in the momentum equation. Specifically, a small repulsive force is applied to each particle pair in the tensile region, with the magnitude of the force increasing as the particle spacing decreases. This approach helps prevent particle overlap and clustering, thereby addressing tensile instability.

---

* Corresponding author.
E-mail address: lourenco@hku.hk (S.D.N. Lourenço).

https://doi.org/10.1016/j.compgeo.2025.107139
Received 21 November 2024; Received in revised form 8 January 2025; Accepted 6 February 2025

In two-dimensional (2D) scenarios, the artificial stress method has been widely adopted and proven effective in mitigating tensile instability (Bui et al., 2008; Bui and Nguyen, 2021; Lian et al., 2022). Nevertheless, since artificial stress is derived under 2D conditions (Gray et al., 2001), its derivation involves operations such as matrix diagonalization and coordinate system rotation, which makes its extension to three-dimensional (3D) scenarios complex, as noted in the literature (Bui and Nguyen, 2021; Zhang et al., 2024a, 2025b). In addition, the artificial stress method is considered highly dissipative (Zhang et al., 2024a), which results in excessive energy decay and makes it unsuitable for long-duration simulations. Another issue is that the artificial stress method involves two coefficients that may require manual adjustment for different cases.

To address the aforementioned issues, this study introduces the transport-velocity formulation (TVF) (Adami et al., 2013; Zhang et al., 2017a; Zhu et al., 2021; Zhang et al., 2025a), commonly used in SPH simulations of fluids to prevent tensile instability, into the modeling of granular materials. The TVF proposed by Adami et al. (2013) was designed to mitigate tensile instability by introducing a constant background pressure. Zhang et al. (2017a) generalized the TVF for free-surface flows by introducing a variable background pressure instead of a constant one, and by adopting a shortened smoothing length to address free-surface problems. Although the background pressure-based TVF improves computational stability, its effectiveness is influenced by the chosen background pressure and time step sizes. Later, the TVF was reformulated by using an advection term by Zhu et al. (2021) based on local particle consistency, which adjusts particle positions to achieve a uniform distribution. Specifically, the position of each particle is modified to meet the normalization condition, which guarantees that the kernel's integral over the support domain sums to unity. This consistency-driven formulation has been shown to improve the stability and accuracy of SPH simulations for inner flows (Zhu et al., 2021). Recently, this consistency-driven approach has undergone further optimization (Wang et al., 2024; Zhang et al., 2025a); however, its applicability remains restricted to inner particles.

Since most problems involving large deformations of granular materials include free surfaces, we build upon the latest version of TVF (Zhang et al., 2025a) and unify its applicability from inner particles alone to both inner and free-surface particles, referring to this as the unified transport-velocity formulation (UTVF). The UTVF is designed to address tensile instability in cohesive granular materials, particularly in 3D scenarios, where the artificial stress method is less effective. The proposed UTVF, along with Riemann-SPH (Zhang et al., 2017b, 2024c), is validated through several benchmark tests involving fluids and elastic materials with known analytical solutions, including the evolution of an elliptical water drop, a rotating square patch, and an oscillating beam, demonstrating its convergence, stability, and accuracy. Additionally, some results are compared with those obtained using the artificial stress method and another commonly used particle regularization technique, the particle shifting scheme (Xu et al., 2009; Khayyer et al., 2017). The UTVF is then applied to the simulation of cohesive granular material failure and granular flows in both 2D and 3D settings, demonstrating its effectiveness in eliminating tensile instability and enhancing the stability and accuracy of SPH simulations.

We have developed and released our open-source code to support simulations of cohesive granular materials. The code is publicly accessible through the SPHinXsys library (Zhang et al., 2021b), available at https://www.sphinxsys.org/. The structure of this paper is as follows. Section 2 outlines the governing equations and constitutive models for fluids, elastic solids, and cohesive granular materials. Section 3 details the SPH discretization approach for these materials, reviews previous forms of transport-velocity formulations, and introduces the proposed UTVF. Section 4 validates the UTVF through benchmark tests, while Section 5 illustrates its application to granular material simulations. Finally, Section 6 summarizes the findings and presents the conclusions.

2. Governing equations and constitutive relations

This section presents the governing equations and constitutive models for granular materials. The governing equations for fluids and elastic solids are also briefly outlined, as they are employed in the validation cases in Section 4.

2.1. Fluids

In the Lagrangian framework, the governing equations of fluids include the conservation of mass and momentum. When materials are incompressible and viscosity is neglected, these equations are expressed as

$$\frac{\mathrm{d}\rho}{\mathrm{d}t} = -\rho\nabla\cdot\mathbf{v} \tag{1}$$

$$\frac{\mathrm{d}\mathbf{v}}{\mathrm{d}t} = -\frac{1}{\rho}\nabla\cdot p + \mathbf{g} \tag{2}$$

where ρ is the density, $\mathbf{v}$ is velocity, p is the pressure, and $\mathbf{g}$ is the body force. The continuity Eq. (1) is the same for other materials, i.e., elastic solids and granular materials.

To simulate incompressible flow under the weakly compressible approximation (Monaghan, 1994; Morris et al., 1997), an artificial isothermal equation of state is employed to complete the formulation of Eq. (2)

$$p = c_0^2(\rho - \rho_0) \tag{3}$$

where ρ_0 is the initial density and c_0 is the sound speed. Generally, in fluid simulations, when an artificial sound speed of $c_0 = 10\left|\mathbf{v}_{max}\right|$ is applied (where $\mathbf{v}_{max}$ represents the anticipated maximum flow velocity), the density fluctuates by approximately 1% (Morris et al., 1997).

2.2. Elastic solids

The momentum equation for elastic solids is given by

$$\frac{\mathrm{d}\mathbf{v}}{\mathrm{d}t} = \frac{1}{\rho}\nabla\cdot\boldsymbol{\sigma} + \mathbf{g} \tag{4}$$

where $\boldsymbol{\sigma}$ is the Cauchy stress tensor. The total stress tensor $\boldsymbol{\sigma}$ can be decomposed into the sum of hydrostatic pressure and shear stress, as illustrated below.

$$\boldsymbol{\sigma} = -p\mathbf{I} + \boldsymbol{\sigma}^s \tag{5}$$

where $\mathbf{I}$ is the identity tensor, p is the pressure and can be solved by Eq. (3) under the weakly compressible assumption (Gray et al., 2001; Zhang et al., 2017a), and $\boldsymbol{\sigma}^s$ is the shear stress tensor. The sound speed for solids is defined as

$$c_0 = \sqrt{\frac{E}{3(1-2\nu)\rho_0}} \tag{6}$$

where E is the Young's modulus, and ν is the Poisson's ratio. Shear stress is derived from the integral of the shear stress rate $\dot{\boldsymbol{\sigma}}^s$.

$$\boldsymbol{\sigma}^s = \int_0^t \dot{\boldsymbol{\sigma}}^s \mathrm{d}t \tag{7}$$

The shear stress rate $\dot{\boldsymbol{\sigma}}^s$ is defined by the constitutive relation of the material. For linear elastic materials, the constitutive relation is given by

$$\dot{\boldsymbol{\sigma}}^s = 2G\dot{\boldsymbol{\varepsilon}}^s \tag{8}$$

where G is the shear modulus, and $\dot{\boldsymbol{\varepsilon}}^s = \dot{\boldsymbol{\varepsilon}} - \frac{1}{d}tr(\dot{\boldsymbol{\varepsilon}})\mathbf{I}$ is the shear strain rate, with d being the dimension of the space. The strain rate tensor $\dot{\boldsymbol{\varepsilon}}$ is defined as

$$\dot{\boldsymbol{\varepsilon}} = \frac{1}{2}\left[\nabla\mathbf{v} + (\nabla\mathbf{v})^T\right] \tag{9}$$

where $\nabla\mathbf{v}$ is the velocity gradient tensor, and $(\cdot)^T$ denotes the transpose of a tensor.

2.3. *Cohesive granular materials*

The elastic-perfectly plastic Drucker–Prager constitutive model is employed to describe the elastoplastic behavior of granular materials (Drucker and Prager, 1952; Borja, 2013). Although some rate-dependent constitutive models, such as the $\mu(I)$-rheological constitutive model (Jop et al., 2006), are also commonly used to describe the motion of granular materials (Lemiale et al., 2011; Hurley and Andrade, 2017; Madraki et al., 2017), SPH studies often assume cohesionless materials (Yang et al., 2021; Zhu et al., 2022) when employing rheological constitutive models to facilitate comparison with experimental results. However, cohesionless granular materials do not exhibit tensile instability, and therefore the UTVF scheme proposed in this study is not required in such cases. Accordingly, this study adopts the Drucker–Prager constitutive model, which is widely used in SPH simulations (Bui et al., 2008; Nguyen et al., 2017; Bui and Nguyen, 2021; Feng et al., 2021; Zhang et al., 2024c). Comparisons are conducted with experimental results under cohesionless conditions and with previous numerical results, to validate the constitutive model is correctly implemented in the SPH code. When cohesion is considered, we demonstrate that tensile instability is completely eliminated by the UTVF scheme, and compare the results with those obtained using the artificial stress method (Bui et al., 2008) and the particle shifting scheme (Lallemand et al., 2025).

The momentum equation for granular materials can be represented by Eq. (4). Unlike elastic solids, where stress tensor $\boldsymbol{\sigma}$ is decomposed into pressure and the shear stress tensor $\boldsymbol{\sigma}^s$, with pressure estimated with equation of state, the total stress tensor $\boldsymbol{\sigma}$ for plastic solids is calculated directly based on constitutive relation, as pressure is also linked to the yield behavior in the Drucker–Prager model.

For non-associate flow rule, the stress rate $\dot{\boldsymbol{\sigma}}$ is given by Borja (2013)

$$\dot{\boldsymbol{\sigma}} = 2G\dot{\boldsymbol{\varepsilon}}_n + K\mathrm{tr}(\dot{\boldsymbol{\varepsilon}}_n)\mathbf{I} - \dot{\gamma}\left(3K\alpha_\phi\mathbf{I} + \frac{G}{\sqrt{J_2}}\boldsymbol{\sigma}_n^s\right) + \boldsymbol{\sigma}_n\cdot\dot{\boldsymbol{\omega}}_n^T + \dot{\boldsymbol{\omega}}_n\cdot\boldsymbol{\sigma}_n \tag{10}$$

with the following yield criterion f and plastic potential function g.

$$f(I_1, J_2) = \alpha_\phi I_1 + \sqrt{J_2} - k_c \tag{11}$$

$$g(I_1, J_2) = \alpha_\psi I_1 + \sqrt{J_2} \tag{12}$$

where the subscript n indicates the time step n. $\boldsymbol{\sigma}^s = \boldsymbol{\sigma} - \frac{1}{3}\mathrm{tr}(\boldsymbol{\sigma})\mathbf{I}$ is the deviatoric stress tensor. K is the bulk modulus and $\dot{\boldsymbol{\omega}} = \frac{1}{2}\left[\nabla\boldsymbol{v} - (\nabla\boldsymbol{v})^T\right]$ is the spin tensor. $I_1 = \mathrm{tr}(\boldsymbol{\sigma})$ and $J_2 = \frac{1}{2}\boldsymbol{\sigma}^s : \boldsymbol{\sigma}^s$ are the first and second invariant of $\boldsymbol{\sigma}$, respectively. The Jaumann stress rate $\dot{\boldsymbol{\sigma}}$ is a commonly adopted approach in SPH-related studies (Bui et al., 2008; Nguyen et al., 2017; Feng et al., 2021). However, it has been shown to exhibit oscillatory behavior under simple shear conditions (Dienes, 1979), as also mentioned by del Castillo et al. (2024). Interestingly, del Castillo et al. (2024)'s investigation further demonstrates that such oscillations were absent in SPH simulations involving both simple shear and large deformation scenarios. Alternatively, other objective stress rates, such as those derived from the Lie derivative (Borja and Tamagnini, 1998), may also be considered in this context.

γ in Eq. (10) is the plastic multiplier and can be determined by the consistency condition. The change rate $\dot{\gamma}$ of the plastic multiplier is given by

$$\dot{\gamma} = \frac{3\alpha_\phi K\mathrm{tr}(\dot{\boldsymbol{\varepsilon}}_n) + (G/\sqrt{J_2})\boldsymbol{\sigma}_n^s : \dot{\boldsymbol{\varepsilon}}_n}{9\alpha_\phi K\alpha_\psi + G} \tag{13}$$

α_ϕ, k_c and α_ψ are material constants in Drucker–Prager model, which are defined as (Borja, 2013; Nguyen et al., 2017)

$$\alpha_\phi = \frac{\tan\phi}{\sqrt{9 + 12\tan^2\phi}}, k_c = \frac{3c}{\sqrt{9 + 12\tan^2\phi}}, \alpha_\psi = \frac{\tan\psi}{\sqrt{9 + 12\tan^2\psi}} \tag{14}$$

Here, c, ϕ, and ψ are cohesion, friction angle, and dilation angle, respectively. Then the trial stress at the new time step $n+1$ can be obtained by

$$\boldsymbol{\sigma}_{n+1}^{trial} = \boldsymbol{\sigma}_n + \dot{\boldsymbol{\sigma}}\Delta t \tag{15}$$

A two-step elastic predictor-plastic corrector scheme, known as the return mapping algorithm (Simo and Hughes, 2006; Bui et al., 2008; Borja, 2013), is employed to return the trial stress $\boldsymbol{\sigma}_{n+1}^{trial}$ to the yield surface and get the final stress $\boldsymbol{\sigma}_{n+1}$.

3. Numerical method

3.1. *SPH discretization*

3.1.1. *Fluids*

A low-dissipation Riemann solver (Zhang et al., 2017b) is introduced to discretize the continuity and momentum equation for fluids, as shown

$$\frac{\mathrm{d}\rho_i}{\mathrm{d}t} = 2\rho_i\sum_j \frac{m_j}{\rho_j}(\mathbf{v}_i - \mathbf{v}^*)\cdot\nabla_i W_{ij} \tag{16}$$

$$\frac{\mathrm{d}\mathbf{v}_i^p}{\mathrm{d}t} = -2\frac{1}{\rho_i}\sum_j \frac{m_j}{\rho_j}P^*\nabla_i W_{ij} \tag{17}$$

Here, $\mathbf{r}$ and h are the particle position and smoothing length, respectively. $W_{ij} = W(\mathbf{r}_i - \mathbf{r}_j, h)$ is the kernel function, and m is the particle mass. The subscripts i and j are particle numbers. The term $\nabla_i W_{ij} = \frac{\partial W(r_{ij},h)}{\partial r_{ij}}\mathbf{e}_{ij}$ is the gradient of the kernel function W_{ij}. $r_{ij} = |\mathbf{r}_i - \mathbf{r}_j|$ is the distance between particles i and j. The unit vector directed from particle j to particle i is represented by $\mathbf{e}_{ij}$. The superscript p in $\frac{\mathrm{d}\mathbf{v}_i^p}{\mathrm{d}t}$ indicates this is pressure-induced acceleration, as opposed to shear stress-induced acceleration in elastic solids.

According to Zhang et al. (2017b), the variables $\mathbf{v}^*$ and P^* are the solutions to an inter-particle Riemann problem, and are defined as (Zhang et al., 2017b)

$$\begin{cases} \mathbf{v}^* = U^*\mathbf{e}_{ij} + \left(\overline{\mathbf{v}}_{ij} - \overline{U}\mathbf{e}_{ij}\right) \\ P^* = \dfrac{\rho_L c_L P_R + \rho_R c_R P_L + \beta\rho_L c_L \rho_R c_R (U_L - U_R)}{\rho_L c_L + \rho_R c_R} \\ U^* = \dfrac{\rho_L c_L U_L + \rho_R c_R U_R + P_L - P_R}{\rho_L c_L + \rho_R c_R} \end{cases} \tag{18}$$

Here, $\overline{\mathbf{v}}_{ij} = \frac{1}{2}\left(\mathbf{v}_i + \mathbf{v}_j\right)$ and $\overline{U} = \frac{1}{2}\left(U_L + U_R\right)$. c_L and c_R are the sound speed. The subscripts L and R denote the left and right states from Riemann problem, and are defined as

$$\begin{cases} \left(\rho_L, U_L, P_L, c_L\right) = \left(\rho_i, -\mathbf{v}_i\cdot\mathbf{e}_{ij}, p_i, c_{0i}\right) \\ \left(\rho_R, U_R, P_R, c_R\right) = \left(\rho_j, -\mathbf{v}_j\cdot\mathbf{e}_{ij}, p_j, c_{0j}\right) \end{cases} \tag{19}$$

The dissipation limiter β is given by Zhang et al. (2017b)

$$\beta = \min\left\{\eta\max\left[\frac{(P_L + P_R)(U_L - U_R)}{\rho_L c_L + \rho_R c_R}, 0\right], 1.0\right\} \tag{20}$$

where η is a coefficient, which is used to modulate dissipation when the fluid is under the action of a compression wave ($U_L \geq U_R$), typically set to 3 for fluids (Zhang et al., 2017b).

3.1.2. *Elastic solids*

For elastic solids, the continuity equation does not require the introduction of the Riemann solver (Zhang et al., 2024b). The continuity equation is discretized as

$$\frac{\mathrm{d}\rho_i}{\mathrm{d}t} = \rho_i\sum_j \frac{m_j}{\rho_j}\mathbf{v}_{ij}\cdot\nabla_i W_{ij} \tag{21}$$

where $\mathbf{v}_{ij} = \mathbf{v}_i - \mathbf{v}_j$. The pressure-induced acceleration for elastic solids is the same with that for fluids (as shown in Eq. (17)), except the dissipation limiter is set to $\beta = 1$ (Zhang et al., 2024b). The shear stress-induced acceleration for elastic solids is given by

$$\frac{d\mathbf{v}_i^s}{dt} = \frac{1}{\rho_i}\sum_j \frac{m_j}{\rho_j}\left(\boldsymbol{\sigma}_i^s + \boldsymbol{\sigma}_j^s\right)\cdot\nabla_i W_{ij} \tag{22}$$

The velocity gradient in Eq. (9) is discretized as (Espanol and Revenga, 2003)

$$\nabla\mathbf{v}_i = \sum_j \mathbf{v}_{ij}\otimes\left(\mathbf{B}_i\nabla_i W_{ij}\right)V_j \tag{23}$$

The correction matrix for the kernel gradient, $\mathbf{B}_i$, is defined as (Randles and Libersky, 1996; Ren et al., 2023)

$$\mathbf{B}_i = -\left(\sum_j \mathbf{r}_{ij}\otimes\nabla_i W_{ij}V_j\right)^{-1} \tag{24}$$

where V_j is the volume of particle j, and $\mathbf{r}_{ij} = \mathbf{r}_i - \mathbf{r}_j$.

3.1.3. Cohesive granular materials

(Zhang et al., 2024c) were the first to introduce the Riemann problem into the SPH simulation of granular materials to incorporate numerical dissipation as a substitute for artificial viscosity terms. They employed a low-dissipation Riemann solver to reduce numerical dissipation, thereby addressing the issue of excessive dissipation that might be introduced by artificial viscosity terms. The accuracy of this method was demonstrated through comparisons with previous results, and it was shown that using a Riemann solver does not reduce computational efficiency compared to methods using the artificial viscosity term (Zhang et al., 2024c). According to Zhang et al. (2024c), the discretization of the continuity equation for granular materials is the same as that for fluids, as shown in Eq. (16). The discretization of momentum equation is given by Zhang et al. (2024c, 2025b)

$$\frac{d\mathbf{v}_i}{dt} = 2\frac{1}{\rho_i}\sum_j \frac{m_j}{\rho_j}\boldsymbol{\sigma}^*\cdot\nabla_i W_{ij} + \mathbf{g} \tag{25}$$

The $\boldsymbol{\sigma}^*$ is expressed as (Zhang et al., 2024c)

$$\boldsymbol{\sigma}^* = \overline{\boldsymbol{\sigma}}_{ij}^s - P^*\mathbf{I} \tag{26}$$

Here, $\overline{\boldsymbol{\sigma}}_{ij}^s = (\boldsymbol{\sigma}_i^s + \boldsymbol{\sigma}_j^s)/2$ is the particle-average shear stress between particles i and j. The pressure P^* is determined by the Riemann solver, as shown in Eq. (18). The hydrostatic pressure of particle i can be obtained by the trace of total stress tensor and $P_i = -\frac{1}{3}\mathrm{tr}(\boldsymbol{\sigma}_i)$ (Zhang et al., 2024c). The coefficient η in the dissipation limiter (Eq. (20)) for granular materials is set to $20d$ according to Zhang et al. (2024c), with d being the space dimension.

A stress diffusion term is introduced in the constitutive equation of Drucker–Prager model to ensure a smooth stress distribution. Further details on this term can be found in the Ref. (Feng et al., 2021).

3.2. Previous transport-velocity formulations

In the work of Adami et al. (2013) and Zhang et al. (2017a), a transport (or advection) velocity $\widetilde{\mathbf{v}}$ is introduced to replace the momentum velocity. This velocity is obtained at every time step Δt by

$$\widetilde{\mathbf{v}}_i(t+\Delta t) = \mathbf{v}_i(t) + \left(\frac{\widetilde{d\mathbf{v}_i}}{dt} - \frac{1}{\rho_i}\nabla p_b\right)\Delta t \tag{27}$$

where p_b is a background pressure. Although the gradient of a constant background pressure is zero, the SPH discretization of ∇p_b under irregular particle distributions does not vanish due to the lack of zero-order consistency, thereby resulting in a non-zero contribution (Adami et al., 2013).

Zhu et al. (2021) improved this background pressure-based transport velocity method by proposing a consistency-driven particle-advection formulation. The advection velocity is modified to

$$\widetilde{\mathbf{v}}_i(t+\Delta t) = \mathbf{v}_i(t) + \left[\frac{\widetilde{d\mathbf{v}_i}}{dt} + \frac{2\Delta\mathbf{r}_i}{(\Delta t)^2}\right]\Delta t \tag{28}$$

where the introduced extra advection term $\Delta\mathbf{r}_i$ is determined by local particle consistency, and is defined as

$$\Delta\mathbf{r}_i = \chi_i E_i \sum_j \nabla_i W_{ij} V_j \tag{29}$$

where $\chi_i = \left[\left(\sum_j \nabla_i W_{ij} V_j\right)^2 + \sum_j \left(\nabla_i W_{ij} V_j\right)^2\right]^{-1}$ is a positive value and E_i is the local integration error estimated based on the normalization (unity) condition of particle approximation (Zhu et al., 2021). With Eq. (28), the position of each particle is adjusted to meet the normalization condition, ensuring that the integral of the kernel over the support domain equals unity.

The recent work by Zhang et al. (2025a) simplifies the advection term $\Delta\mathbf{r}_i$ with

$$\Delta\mathbf{r}_i = 2\alpha h^2 \sum_j \nabla_i W_{ij} V_j \tag{30}$$

Here, the coefficient α can be generally set to 0.2 to ensure numerical stability (Zhang et al., 2025a), and the smoothing length h is used to scale the advection term. Together with the momentum velocity, the term $\Delta\mathbf{r}_i$ is iteratively applied to correct zero-order integration errors by adjusting particle positions.

3.3. Unified transport-velocity formulation

Similar to Eq. (29), the essence of Eq. (30) is also to adjust particle positions within the support domain, determined by each particle's smoothing length h, to achieve zero-order consistency of the local particles, thereby enhancing numerical stability. This method is effective for inner particles (i.e., particle i_1 in Fig. 1) where the support domain is complete, but presents significant issues for free-surface particles (i.e., near-surface particle i_2 and outermost-surface particle i_3 in Fig. 1) where the kernel function is truncated. Considering both computational efficiency and accuracy, h/dp (dp is the initial particle spacing) is typically less than 1.5 (Oger et al., 2007) and is set to 1.3 throughout this paper, meaning that two layers of particles on the free surface will experience kernel truncation and are thus labeled as free-surface particles, as shown in Fig. 1. For free-surface particles, if the extra advection term $\Delta\mathbf{r}_i$ is applied, free-surface particles will move in a direction away from other particles under the requirement of local zero-order consistency. For example, particle i_3 in Fig. 1 will move in the direction of $\Delta\mathbf{r}_{i_3}$, leading to highly inaccurate computational results.

Therefore, in previous studies, transport-velocity corrections are applied only to inner particles, while free-surface particles are left uncorrected (Ren et al., 2023; Zhang et al., 2025a). However, numerical instabilities can still occur in fluid simulations with longer computation times, and such errors become even more pronounced in solid simulations (please refer to Section 4 for details.). Building on this, we have extended the latest transport-velocity formulation, as shown in Eq. (30), to accommodate free surfaces, thus facilitating long-term stable simulations for free-surface problems.

Firstly, the free-surface particles, include outermost-surface particles and near-surface particles, need to be identified. The outermost-surface particles are classified if $\nabla\cdot\mathbf{r} < 0.75d$ (Lind et al., 2012; Khayyer et al., 2017), with d being the space dimension. The divergence of the particle position is given by Lee et al. (2008)

$$\nabla\cdot\mathbf{r}_i = \sum_j \mathbf{r}_{ij}\cdot\nabla_i W_{ij} V_j \tag{31}$$

The method for identifying near-surface particles is adapted from the Refs. (Khayyer et al., 2017; Zhang et al., 2023). Particle i is considered a near-surface particle if there exists any particle j in its neighborhood that satisfies both of the following conditions: (1)

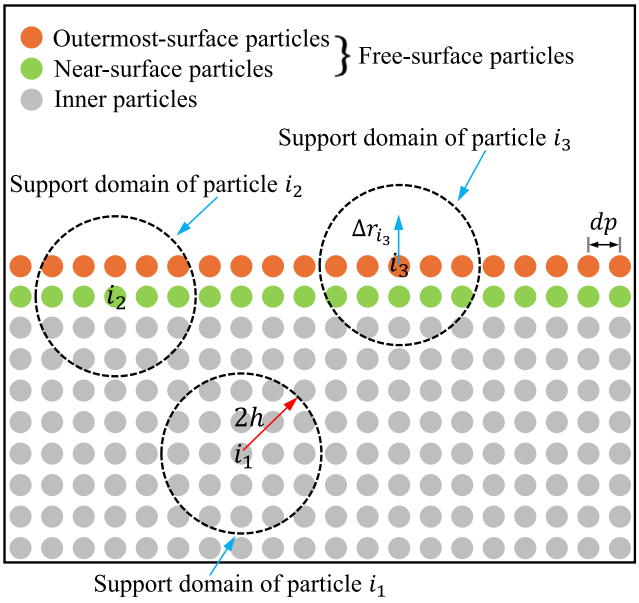

Fig. 1. Illustration of inner and free-surface particles.

particle j is an outermost surface particle; (2) the distance between particle i and particle j is less than the smoothing length h.

The normal direction of the free-surface particles is then calculated following the method of Brackbill et al. (1992).

$$\mathbf{n}_i = \frac{\nabla C_i}{|\nabla C_i|} \tag{32}$$

where ∇C_i is the gradient of color function C_i, and is defined as

$$\nabla C_i = \sum_j \widetilde{C}_{ij} \nabla_i W_{ij} V_j \tag{33}$$

with

$$\widetilde{C}_{ij} = \frac{\rho_i}{\rho_i + \rho_j} C_i + \frac{\rho_j}{\rho_i + \rho_j} C_j \tag{34}$$

where $C_i = 1$. $C_j = 1$ if particle j and particle i are of the same material, and $C_j = 0$ if particle j and particle i are of different materials (Hu and Adams, 2006). For this study, at the free surface, the neighboring particle j and particle i belongs to the same material, Eq. (33) can be simplified to $\nabla C_i = \sum_j \nabla_i W_{ij} V_j$. The correction matrix for kernel gradient $\mathbf{B}_i$, as shown in Eq. (24), is used to improve the accuracy of normal direction by Khayyer et al. (2017)

$$\widetilde{\mathbf{n}}_i = \frac{\mathbf{B}_i \cdot \nabla C_i}{|\mathbf{B}_i \cdot \nabla C_i|} \tag{35}$$

Inspirited by the optimized particle shifting scheme (Khayyer et al., 2017), the advection position term $\Delta \mathbf{r}_i$ is projected onto the tangential direction for all the free-surface particles.

$$\Delta \mathbf{r}_i^{surface} = \Delta \mathbf{r}_i - \left(\Delta \mathbf{r}_i \cdot \widetilde{\mathbf{n}}_i\right) \widetilde{\mathbf{n}}_i = \left(\mathbf{I} - \widetilde{\mathbf{n}}_i \otimes \widetilde{\mathbf{n}}_i\right) \cdot \Delta \mathbf{r}_i \tag{36}$$

Finally, the advection term using the unified transport-velocity formulation, which is suitable for free surface simulations, is expressed as

$$\Delta \mathbf{r}_i^{UTVF} = \begin{cases} 2\alpha h^2 \sum_j \nabla_i W_{ij} V_j & \text{for inner particles} \\ 2\alpha h^2 \left(\mathbf{I} - \widetilde{\mathbf{n}}_i \otimes \widetilde{\mathbf{n}}_i\right) \cdot \sum_j \nabla_i W_{ij} V_j & \text{for free-surface particles} \end{cases} \tag{37}$$

It should be noted that in certain cases, when particles are splashed, transport-velocity correction is not required. The criteria for identifying splashed particle i follow Khayyer et al. (2017), where $\nabla \cdot \mathbf{r}_i < 0.75d$, and there are no near-surface particles in its neighborhood. Additionally, considering that the calculation of the normal vector would be inaccurate when the number of neighboring particles of particle i is very small, we do not adjust the position of particle i when $\nabla \cdot \mathbf{r}_i < 0.6d$.

Fig. 2 illustrates the effect of UTVF compared to TVF. Initially, a horizontal disturbance of $0.4dp$ ∗rand(−1,1) (Fig. 2b) is applied to each particle based on a uniform lattice particle distribution (Fig. 2a), where rand(−1,1) generates a random real number between −1 and 1. After the random disturbance, some particles cluster together, similar to the particle clustering seen in tensile instability (Gray et al., 2001). TVF resolves particle clustering for the inner particles, creating a uniform particle distribution, but it has no effect on free-surface particles. In contrast, UTVF acts on both inner and free-surface particles simultaneously. In Section 4 and Section 5, we will demonstrate through case studies how the clustering of free-surface particles and the formation of non-physical voids, particularly in solid materials, can significantly affect computational stability and accuracy.

3.4. Time integration scheme

The time step $\triangle t$ is defined as (Zhang et al., 2024c)

$$\triangle t = CFL \frac{h}{c_0 + |\mathbf{v}|_{max}} \tag{38}$$

where $CFL = 0.4$. The position-based Verlet scheme (Zhang et al., 2021a) is utilized for acoustic time integration. The particle position and density are initially updated to the midpoint $n + \frac{1}{2}$ from beginning step n using the following procedure.

$$\begin{cases} \mathbf{r}_i^{n+\frac{1}{2}} = \mathbf{r}_i^{n} + \frac{1}{2} \triangle t \mathbf{v}_i^{n} \\ \rho_i^{n+\frac{1}{2}} = \rho_i^{n} + \frac{1}{2} \triangle t \left(\frac{\mathrm{d}\rho_i}{\mathrm{d}t}\right)^{n} \end{cases} \tag{39}$$

Then the velocity is updated to the new time step $n + 1$.

$$\mathbf{v}_i^{n+1} = \mathbf{v}_i^{n} + \triangle t \left(\frac{\mathrm{d}\mathbf{v}_i}{\mathrm{d}t}\right)^{n+1} \tag{40}$$

where $\left(\mathrm{d}\mathbf{v}_i/\mathrm{d}t\right)^{n+1}$ is estimated from momentum equation. Finally, the particle position and density are advanced to the new time step by

$$\begin{cases} \mathbf{r}_i^{n+1} = \mathbf{r}_i^{n+\frac{1}{2}} + \frac{1}{2} \triangle t \mathbf{v}_i^{n+1} \\ \rho_i^{n+1} = \rho_i^{n+\frac{1}{2}} + \frac{1}{2} \triangle t \left(\frac{\mathrm{d}\rho_i}{\mathrm{d}t}\right)^{n+1} \end{cases} \tag{41}$$

The transport-velocity is utilized for each particle by

$$\widetilde{\mathbf{r}}_i = \mathbf{r}_i + \Delta \mathbf{r}_i^{UTVF} \tag{42}$$

where $\mathbf{r}_i$ and $\widetilde{\mathbf{r}}_i$ are the position vectors before and after applying the transport-velocity term $\Delta \mathbf{r}_i^{UTVF}$, respectively.

4. Benchmark validation

In this section, we use several benchmark cases of fluids and elastic solids with known analytical solutions to validate the proposed UTVF. A fifth-order Wendland kernel (Wendland, 1995) is applied for all cases with $h = 1.3dp$.

4.1. Evolution of an elliptical water drop

A simple benchmark case, specifically the evolution of a circular water drop into an elliptical shape (Monaghan, 1994; Khayyer et al., 2017), is conducted to validate the proposed UTVF for free-surface flows. The results are compared with those obtained using the TVF, as well as other particle regularization techniques, i.e., dynamic stabilization (DS) (Tsuruta et al., 2013), particle shifting (PS) (Xu et al., 2009), and optimized particle shifting (OPS) (Khayyer et al., 2017). The initial radius of the circular drop is 1 m, and it begins to move under the influence of the initial velocity field $(-100x, 100y)$ m/s (as shown in Fig. 3), with x and y being the coordinates of each particle. The fluid

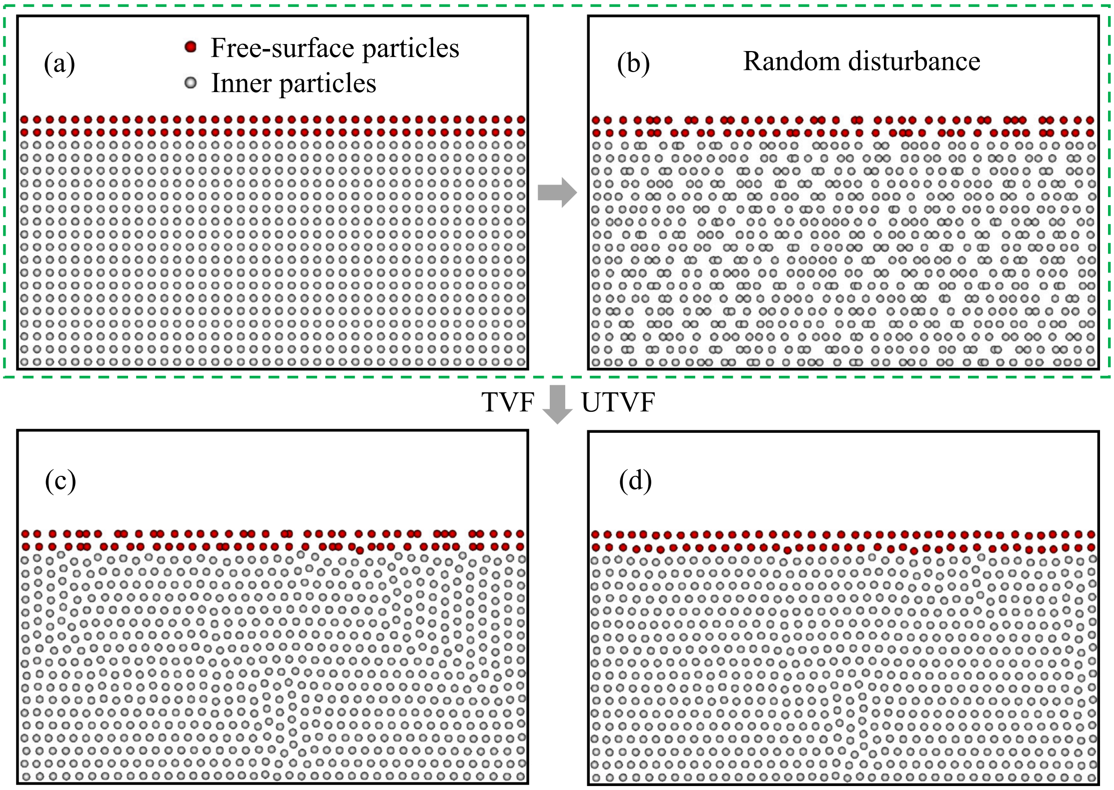

Fig. 2. Comparison of the effects of UTVF and TVF on particle distributions with initial random disturbances: (a) particles in the initial lattice distribution; (b) particles after initial disturbances; (c) particle distribution after applying TVF; (d) particle distribution after applying UTVF.

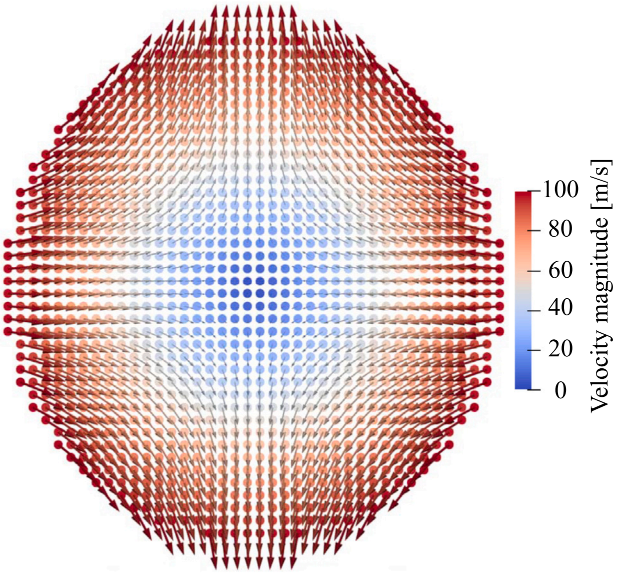

Fig. 3. Elliptical water drop: initial velocity distribution.

density is set to 1000 kg/m^3, and viscosity is not considered. Since there are no external forces throughout the process, theoretically, the linear and angular momentum should be fully conserved.

Fig. 4 presents the particle configuration and pressure distribution of the elliptical drop at $t = 0.008$ s, comparing the results without correction, with the TVF and UTVF methods. Without any correction, both the inner and free-surface particles exhibit irregular distributions, leading to reduced pressure calculation accuracy. Applying the TVF improves the regularity of the inner particle distribution, but particle overlap still persists among the free-surface particles. In contrast, the proposed UTVF ensures a regular distribution for both inner and free-surface particles.

The theoretical evolution of the semi-minor axis and the semi-major axis of the elliptical drop during its motion can be derived (Monaghan, 1994). Fig. 5 illustrates the time evolution of semi-minor and the semi-major axes with different resolutions ($dp = 0.1$ m, 0.05 m, 0.02 m), along with the analytical values for comparison. It can be observed that as the resolution increases (i.e., as dp decreases), the lengths of the semi-axes obtained from numerical calculations gradually converge to the theoretical solution, thereby validating the convergence and accuracy of the proposed method.

The temporal variation of the x-direction linear and angular momentum is shown in Fig. 6. The results from DS, PS, OPS (Khayyer et al., 2017) and TVF are also included for comparison. Both TVF and UTVF, similar to DS, achieve full conservation of linear momentum, while PS and OPS show notable and slight deviations, respectively. UTVF also demonstrates superior angular momentum conservation compared to PS and OPS. Additionally, by regularizing the distribution of both free-surface and inner particles, UTVF can enhance angular momentum conservation compared to TVF, which only applies to inner particles. Although the angular momentum in DS is exactly conserved, we will show in Section 4.2 that DS introduces significant dissipation (Khayyer et al., 2017), leading to poor energy conservation.

4.2. Rotating square patch

In this section, we examine a rotating square water patch with significant free-surface deformation to evaluate the performance of the proposed UTVF method. This benchmark was first proposed in Colagrossi (2005) and has been widely utilized as a standard numerical test for particle-based simulations (Khayyer et al., 2017; Le Touzé et al., 2013).

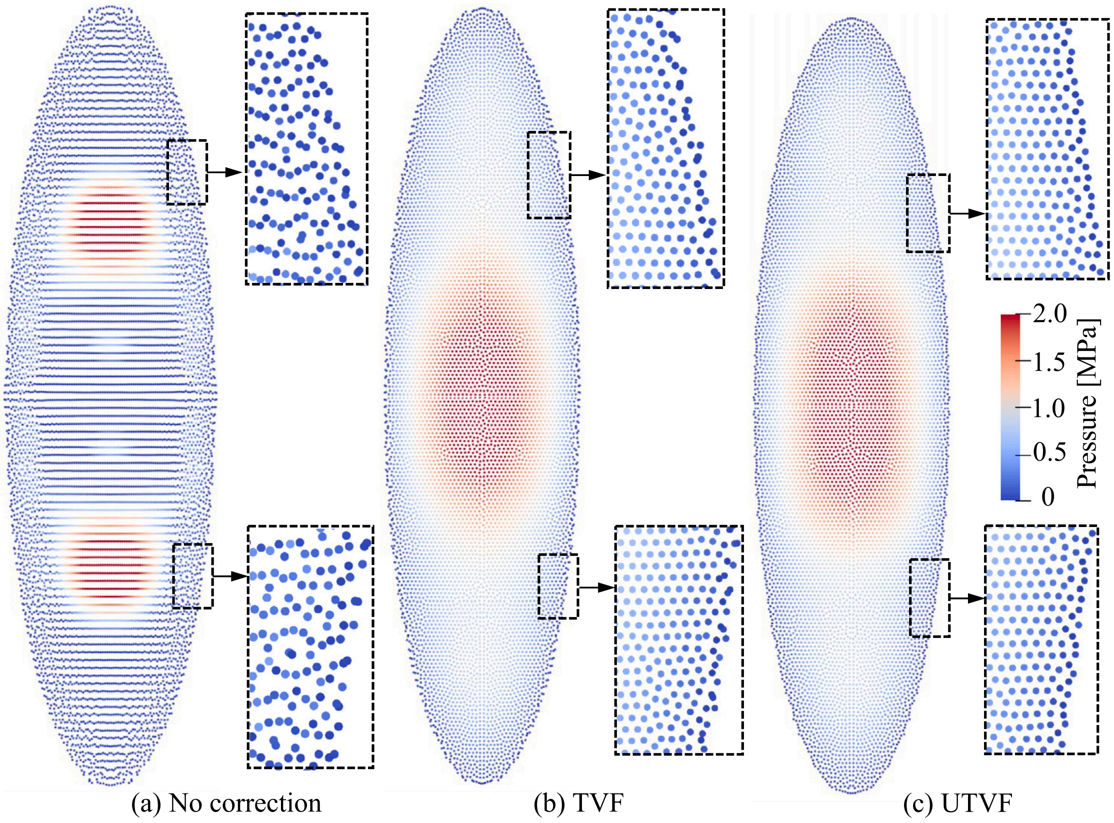

(a) No correction (b) TVF (c) UTVF

Fig. 4. Elliptical water drop: snapshots of the particle configuration and pressure field at $t = 0.008$ s with different numerical schemes, i.e., (a) without correction, (b) with TVF, and (c) with UTVF. Here, $dp = 0.02$ m.

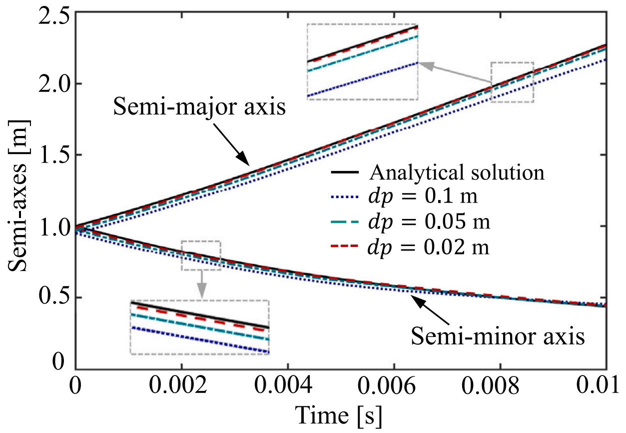

Fig. 5. Elliptical water drop: analytical and numerical results for the time history of the semi-minor and the semi-major axes of the elliptical drop with UTVF.

The initial configuration of the square patch is shown in Fig. 7, with a side length of L. The initial velocity profile, as shown in Fig. 7a, is given by Colagrossi (2005)

$$\begin{cases} v_x(x, y; t = 0) = +\omega y \\ v_y(x, y; t = 0) = -\omega x \end{cases} \tag{43}$$

where ω denotes the angular velocity corresponding to the pure rigid rotation of the fluid patch. The initial pressure distribution is obtained by solving the Poisson equation under the incompressible assumption (Colagrossi, 2005), and is defined as

$$p(x, y; t = 0) = - \rho \sum_{m}^{\infty} \sum_{n}^{\infty} \frac{32\omega^2}{mn\pi^2 \left[(m\pi/L)^2 + (n\pi/L)^2\right]} \sin\left(\frac{m\pi x^*}{L}\right) \sin\left(\frac{n\pi y^*}{L}\right) \quad m, n \in N_{odd} \tag{44}$$

where $x^* = x + L/2$ and $y^* = y + L/2$. In this case, the fluid density $\rho = 1000$ kg/m^3, $L = 1$ m and $\omega = 1$ rad/s.

Fig. 8 shows the particle configuration and pressure distribution at $t\omega = 1.08$ and $t\omega = 2.04$ with TVF (Fig. 8a) and UTVF (Fig. 8b), respectively. The results are compared with the contour obtained using the finite difference method (FDM) (Le Touzé et al., 2013), represented by the black dashed line in Fig. 8. The zoomed-in window on the right side of each subplot clearly shows the particle distribution. It can be observed that the UTVF method significantly improves the regularity of the particle distribution, particularly for free-surface particles, compared to TVF. The profile obtained using the TVF method is similar to that of the UTVF method, both of which agree well with the FDM results.

In this case, since no external forces are applied, the kinetic energy of the square patch should theoretically be conserved. Fig. 9a shows the variation of energy decay, i.e., $(E_K - E_K^0)/E_K^0$, with time, where E_K is the current kinetic energy and E_K^0 is the initial kinetic energy. It can be seen that, compared to the previous DS, PS, and OPS methods (Khayyer et al., 2017), the proposed method in this study exhibits lower energy dissipation and thus improved conservation. Notably, although the results in Section 4.1 show that the DS method ensures complete linear momentum and angular momentum conservation, it introduces significant dissipation, making it unsuitable for long-duration computations. Fig. 9b shows the variation of pressure at the center point over time, which closely matches the reference results derived using a mixed Eulerian–Lagrangian boundary element method (BEM-MEL) (Le Touzé et al., 2013).

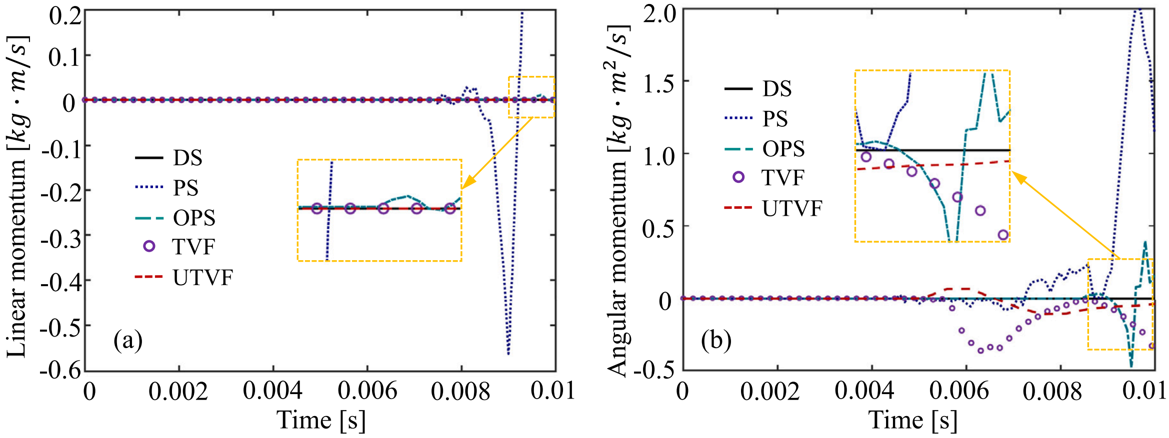

Fig. 6. Elliptical water drop: temporal variation of x-direction (a) linear momentum and (b) angular momentum. The results obtained using the proposed UTVF are compared with those from TVF, DS, PS, and OPS. The data for DS, PS, and OPS are extracted from Khayyer et al. (2017). $dp = 0.01$ m for all simulations.

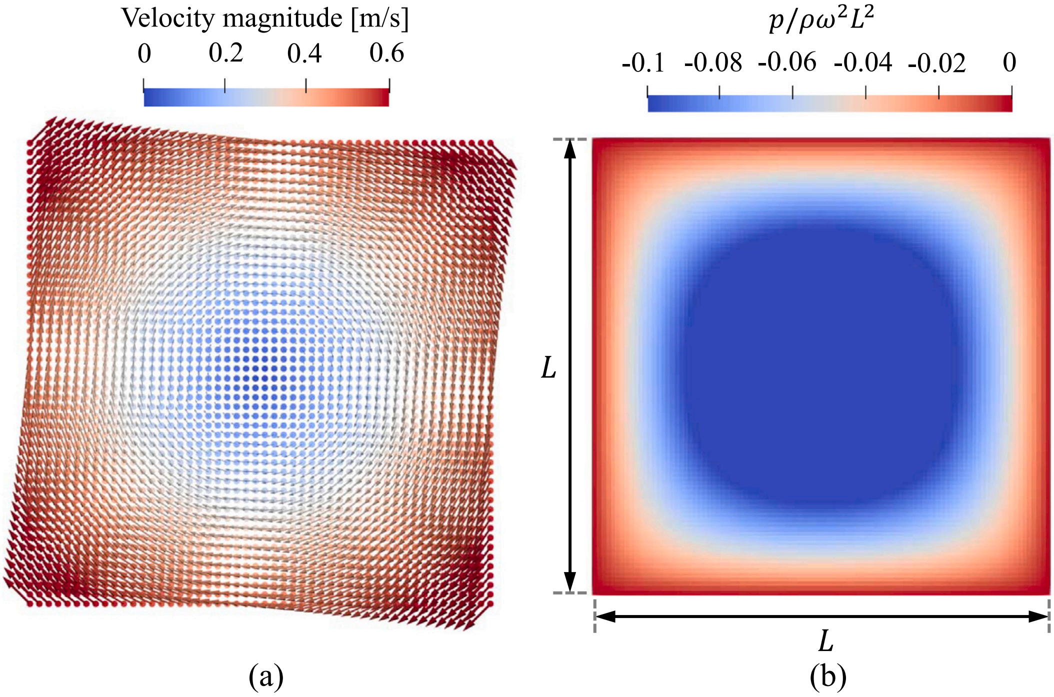

Fig. 7. Rotating square patch: (a) initial velocity distribution; (b) initial pressure distribution.

4.3. Oscillating beam

Next, we use a simple elastic case with a theoretical solution, to further validate the convergence and accuracy of the proposed UTVF method. The previous two fluid cases demonstrated that, compared to TVF, UTVF results in a more uniform distribution of free-surface particles, although it has little impact on the macroscopic deformation. We will further show that such free-surface particle clustering in solid materials can lead to severe consequences. As illustrated in Fig. 10, we first validate the proposed method using an elastic beam with one edge fixed. The results are then compared to existing theoretical (Landau and Lifshitz, 2013) and numerical (Gray et al., 2001; Zhang et al., 2024a) solutions. The beam has a length L and thickness H, with the left edge fixed to create a cantilever configuration. An observation point is placed at the midpoint of the rear end to record the vertical displacement (deflection). The material and dimensional parameters are taken from the literature (Gray et al., 2001; Zhang et al., 2024a), i.e., density $\rho_0 = 1000\ \mathrm{kg/m^3}$, Young's modulus $E = 2$ MPa, Poisson's ratio $\nu = 0.3975$, $L = 0.2$ m, and $H = 0.02$ m. An initial velocity v_y, applied perpendicular to the beam, is given by

$$v_y(x) = v_f c_0 \frac{f(x)}{f(L)} \tag{45}$$

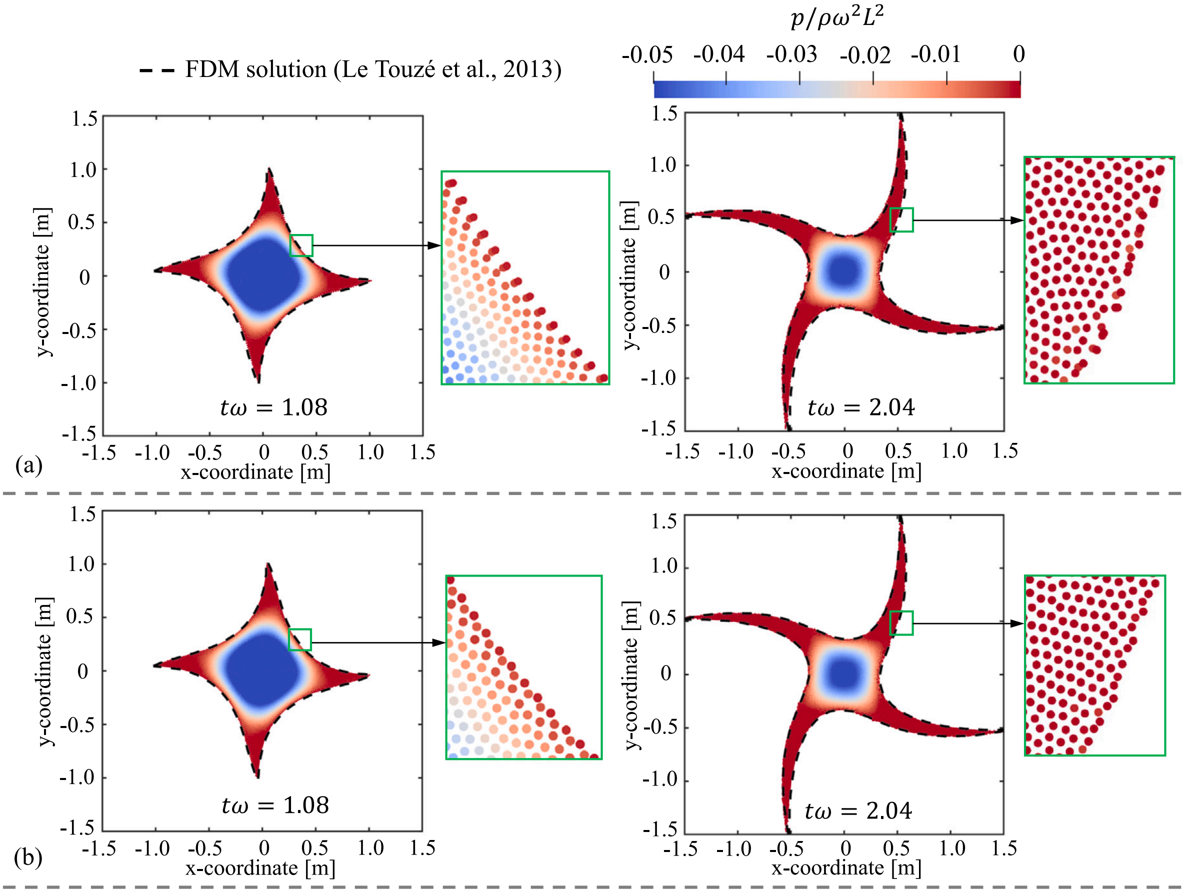

Fig. 8. Rotating square patch: snapshots of the particle configuration and pressure distribution at $t\omega = 1.08$ and $t\omega = 2.04$ with different numerical schemes, i.e., (a) TVF and (b) UTVF. The black dashed line represents the contour obtained using the FDM method (Le Touzé et al., 2013), and $dp = L/100$.

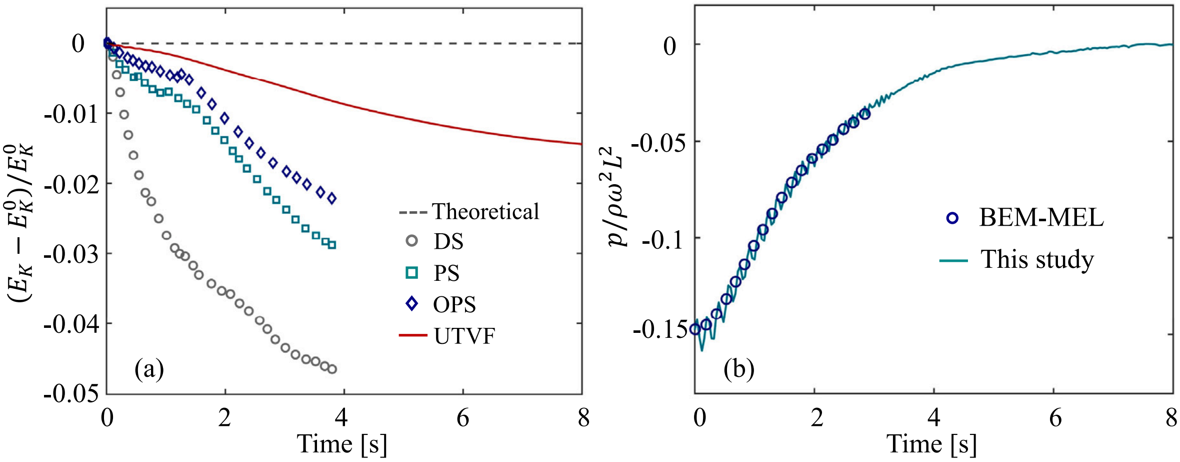

Fig. 9. Rotating square patch: temporal variation of (a) energy decay and (b) pressure at the center of the square patch. The energy decay results obtained using the proposed UTVF are compared with those from TVF, DS, PS, and OPS, with data for DS, PS, and OPS extracted from Ref. (Khayyer et al., 2017). The pressure values are compared with results obtained from BEM-MEL (Le Touzé et al., 2013). $dp = L/100$ for all simulations.

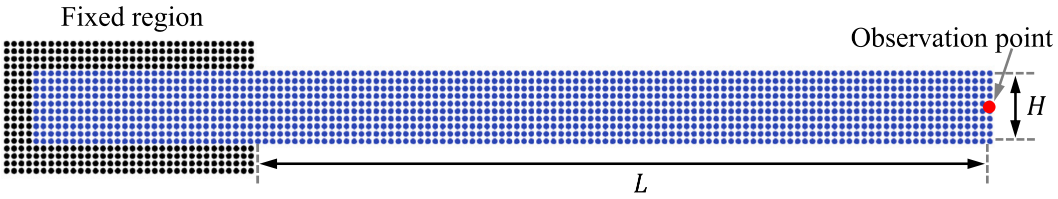

Fig. 10. Oscillating beam: model setup.

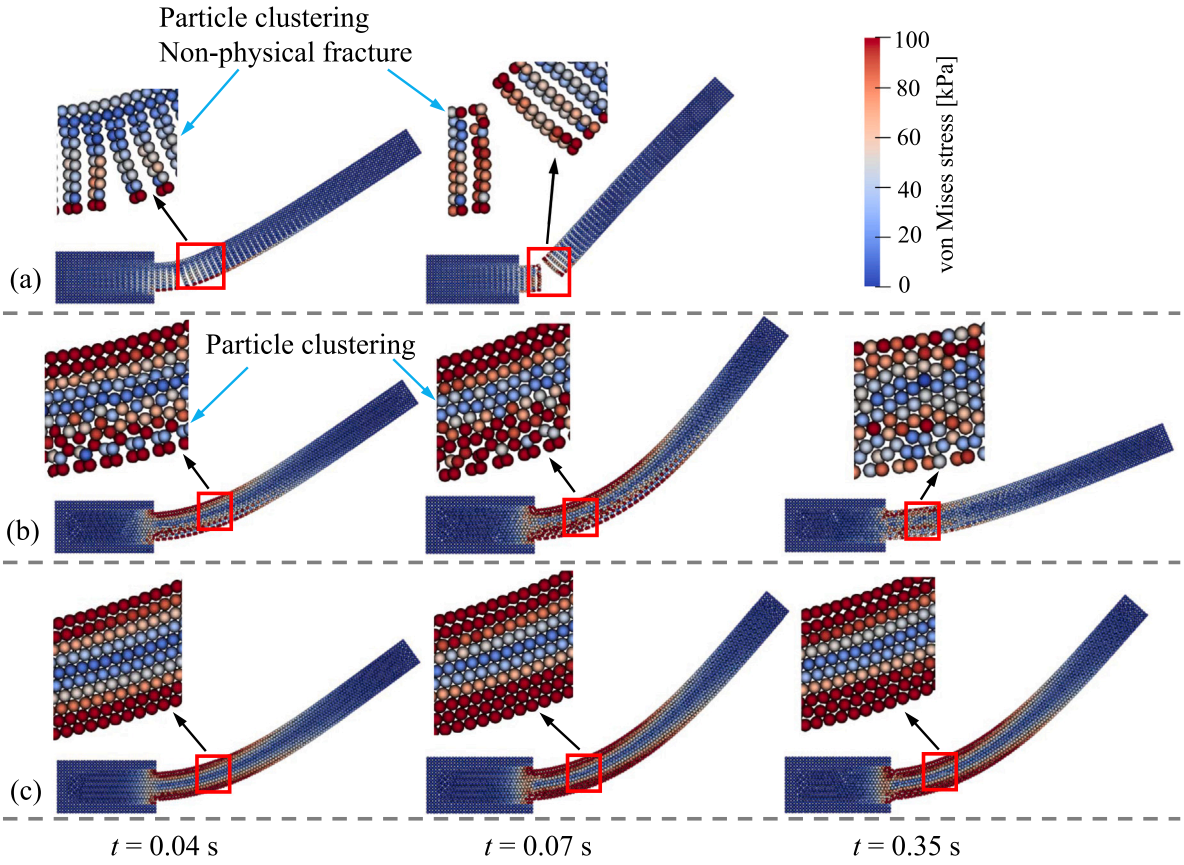

Fig. 11. Oscillating beam: evolution of particle configuration with time (t = 0.04 s, 0.07 s and 0.35 s) for SPH simulations (a) without correction, (b) with TVF, and (c) with UTVF. Here, $v_f = 0.05$, $L = 0.2$ m, $H = 0.02$ m, and $H/dp = 10$. The particles are colored by von Mises stress.

where v_f is a constant that controls the magnitude of initial velocity, c_0 is the sound speed, and $f(x)$ is a function defined as

$$\begin{aligned} f(x) &= (\sin(kL) + \sinh(kL))(\cos(kx) - \cosh(kx)) \\ &\quad -(\cos(kL) + \cosh(kL))(\sin(kx) - \sinh(kx)) \end{aligned} \tag{46}$$

where $kL = 1.875$ is determined by the equation $\cos(kL)\cosh(kL) = -1$. The frequency ω of the oscillating beam is theoretically given by

$$\omega^2 = \frac{EH^2k^4}{12\rho_0(1-\nu^2)} \tag{47}$$

Fig. 11 illustrates the computational results when no correction, TVF, and UTVF are applied. It is evident that without any correction, significant particle clustering and non-physical fractures occur, making further computation difficult. While using TVF addresses the irregular

Table 1
Oscillating beam: comparison of the first oscillation period T obtained from SPH-TVF, the present SPH-UTVF, SPH-AS (Gray et al., 2001) and analytical solutions. Here, $L = 0.2$ m, $H = 0.02$ m and $H/dp = 30$.

v_f	0.001	0.01	0.03	0.05
T (Analytical)	0.254	0.254	0.254	0.254
T (SPH-TVF)	0.275	0.277	0.283	0.284
T (SPH-UTVF)	0.274	0.271	0.271	0.271
T (SPH-AS)	0.273	0.273	0.275	0.278
Error (SPH-TVF)	8.3%	9.1%	11.4%	11.8%
Error (SPH-UTVF)	7.9%	6.7%	6.7%	6.7%
Error (SPH-AS)	7.5%	7.5%	8.3%	9.4%

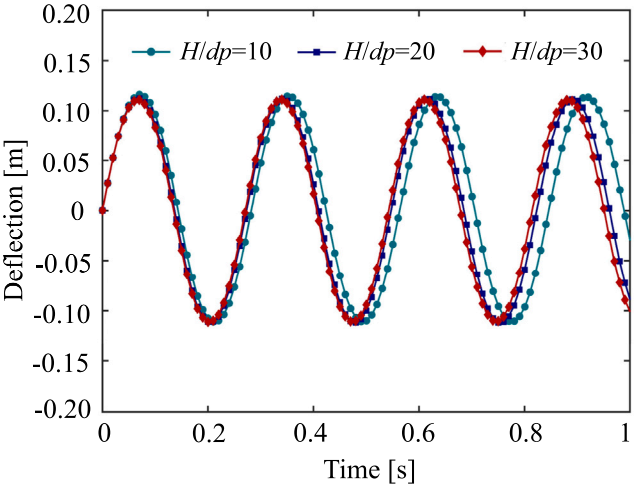

Fig. 12. Oscillating beam: temporal evolution of deflection at various resolutions. Here, $\upsilon_f = 0.05$, $L = 0.2$ m, and $H = 0.02$ m.

distribution of inner particles, free-surface particles still tend to cluster in the tensile region. This clustering affects stress distribution and the deformation behavior of the material. For instance, at $t = 0.35$ s, there is a significant difference between the results of TVF and UTVF. A quantitative analysis of the oscillating period with theoretical solutions will be conducted subsequently. When UTVF is applied, both inner and free-surface particles are distributed uniformly, and the stress distribution is smooth.

The temporal evolution of the deflection at the observation point is shown in Fig. 12 for various resolutions using the present UTVF. It can be observed that as the resolution increases, the difference between adjacent resolutions decreases, indicating the convergence of the present method.

Table 1 shows the first oscillation period T obtained from the present UTVF, TVF, and the analytical solution. For comparison, results from the artificial stress method (SPH-AS) (Gray et al., 2001), commonly used in solid dynamics, have also been included. Clearly, the use of UTVF reduces the error relative to the theoretical value compared to TVF. Additionally, the error of SPH-UTVF is at the same level as that of SPH-AS. While the use of artificial stress can yield relatively accurate periodic values, it introduces significant dissipation. Fig. 13 shows the long-term temporal evolution of elastic strain energy, kinetic energy, and total energy in SPH simulations using both artificial stress and UTVF. When with artificial stress, total energy rapidly decays, whereas the present UTVF method demonstrates improved energy conservation. Additionally, after a certain period in the simulation, the elastic strain energy with artificial stress does not return to zero even when the beam returns to its initial position (where kinetic energy reaches its maximum). This is due to the hourglass issues (Zhang et al., 2024a) in the later stages of the simulation when using artificial stress, which causes a zigzag distribution of particles and stress. As a result, even when the beam returns to its initial position, the stress of some particles remains non-zero, as illustrated in the literature (Zhang et al., 2024a). The study by Zhang et al. (2024a) also demonstrated that in elastic solids, such particle clustering and non-physical fractures are caused by hourglass modes. Nevertheless, this case is presented here to illustrate that the proposed UTVF effectively eliminates these numerical instabilities.

5. Application to granular materials

This section firstly simulates cohesionless granular materials and compares the results with experimental data (Nguyen et al., 2017) to validate the correct implementation of the Drucker–Prager constitutive model. Subsequently, cohesive granular materials are simulated to demonstrate that the proposed UTVF effectively prevents the occurrence of tensile instability. A no-slip wall-boundary condition (Bui et al., 2008; Zhang et al., 2024c) is applied in this section.

Table 2
Material parameters of granular materials.

Parameter	Section 5.1	Section 5.2 & 5.3 & 5.4
Density (kg/m^3)	2040	1850
Young's modulus (MPa)	5.84	1.8
Poisson's ratio	0.3	0.3
Cohesion (kPa)	0	5
Friction angle (°)	21.9	25
Dilation angle (°)	0	0

5.1. 2D granular column collapse

The collapse of a 2D cohesionless granular column is simulated. The model setup is shown in Fig. 14, with material parameters detailed in Table 2 (Nguyen et al., 2017). The numerical simulations are designed to replicate the experimental conditions (Nguyen et al., 2017), where the granular column is released under the influence of self-gravity (gravity acceleration $g = 9.8$ m/s^2). 2D granular flows are examined for model lengths (L) of 0.2 m and 0.1 m separately, while the model height (H) is consistently maintained at 0.1 m. The initial particle spacing is set to $dp = 0.002$ m.

Figs. 15 and 16 illustrate the profiles of the soil column at different times for cases of $L = 0.2$ m and $L = 0.1$ m, respectively, with experimental results (the solid line in green) (Nguyen et al., 2017) included for comparison. The granular flow begins at the front of the column and gradually advances forward until coming to rest at the deposit's toe. Throughout the entire motion process, the current numerical results show good agreement with the experimental data, indicating that the Drucker–Prager constitutive model has been correctly implemented within the present computational framework. This lays a solid foundation for subsequent studies incorporating cohesion to investigate the role of the proposed UTVF scheme in eliminating tensile instability. Fig. 17 illustrates the distribution of the accumulated deviatoric plastic strain in the soil column for the final deposit. A shear band interface is observed, beneath which the particles remain stationary, while the particles above the interface move outward. This observation is also consistent with the experimental results (Nguyen et al., 2017).

5.2. 2D failure of cohesive granular materials

A rectangular soil mass with a length of $L = 4$ m and a height of $H = 2$ m fails under its own weight, following the setup in Bui et al. (2008). Due to the cohesive nature of the soil, severe tensile instability will occur in the tensile region if only the original SPH formulation is used. In this section, we apply the proposed UTVF to this problem and compare the results with those obtained using TVF and the unmodified approach. Literature results based on artificial stress (Bui et al., 2008) and particle shifting (Lallemand et al., 2025) are also included to demonstrate the validity of the findings. The material parameters, consistent with those in Bui et al. (2008), are listed in Table 2.

Fig. 18 shows the simulation results at various time points when no correction, TVF, and UTVF are applied, respectively. In each subplot, an enlarged inset in the lower-left corner clearly shows the local particle distribution. It can be observed that the original SPH, when simulating cohesive granular materials, exhibits severe particle clustering and non-physical fractures in the tensile region, indicating tensile instability. This instability significantly affects the computational results, leading

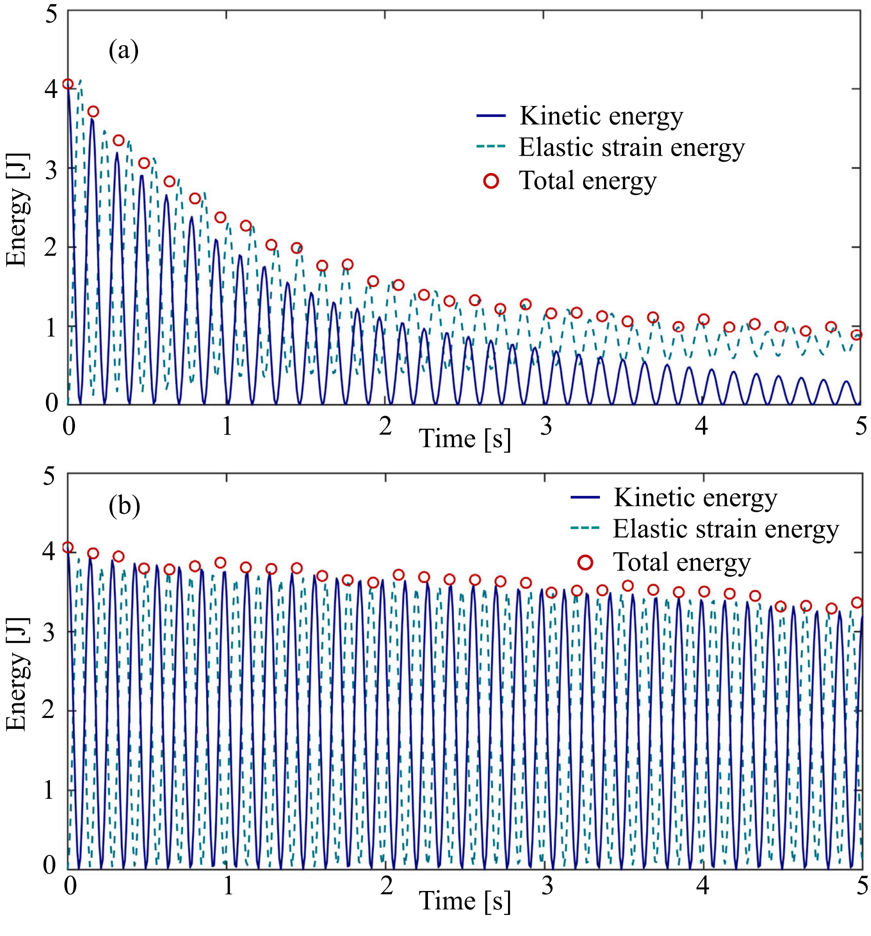

Fig. 13. Oscillating beam: temporal evolution of elastic strain energy, kinetic energy, and total energy for SPH simulations with (a) artificial stress and (b) UTVF. Here, $L = 0.2$ m, $H = 0.02$ m, $H/dp = 10$ and $\mathbf{v}_f = 0.05$.

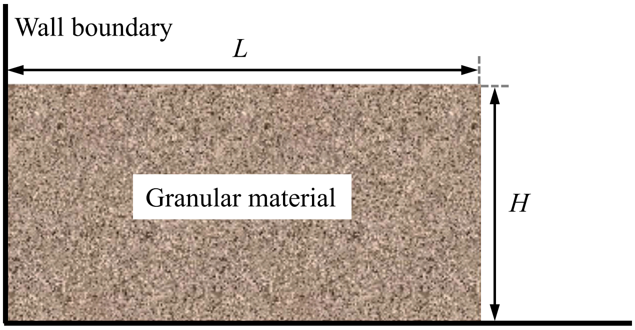

Fig. 14. 2D granular column collapse: model setup.

to an over-prediction of the sliding distance in this case. When TVF is applied, the tensile instability of inner particles is mitigated; however, particle clustering still occurs for free-surface particles. With the present UTVF, tensile instability is completely eliminated for both inner and free-surface particles, resulting in a uniform particle distribution. Upon reaching a stable state ($t = 2$ s), a shear band extending from top to bottom can be observed in the right region, while the area to the left of the shear band remains undisturbed. This result is consistent with findings reported in the literature (Bui et al., 2008; Lallemand et al., 2025).

Fig. 19 shows the external contour of the soil column at $t = 2$ s and includes comparison results from the literature where artificial stress (Bui et al., 2008) and particle shifting (Lallemand et al., 2025) were applied to mitigate tensile instability. Overall, the results from the different methods are consistent. However, a notable distinction is observed with the UTVF method: a step-path failure phenomenon occurs in the sliding region, characterized by an initial descent followed by an upward shift of the soil surface. This feature does not appear in the other methods. In fact, the previous study by Lallemand et al. (2025) have shown that increasing resolution (i.e., decreasing particle spacing dp) can also induce this step-path failure on the soil surface. This can be explained by the analysis of energy decay for UTVF, particle shifting, and artificial stress discussed in Section 4. As illustrated in Fig. 9 and Fig. 13, energy dissipation occurs more rapidly with particle shifting and artificial stress compared to UTVF. This excessive energy dissipation explains why particle shifting and artificial stress do not exhibit step-path failure at the current resolution; in other words, excessive numerical energy decay may obscure certain physical phenomena that should have occurred. As the resolution increases, the effects of these corrections—and thus the associated energy dissipation—diminish, eventually allowing step-path failure to emerge (Lallemand et al., 2025). In contrast, the UTVF

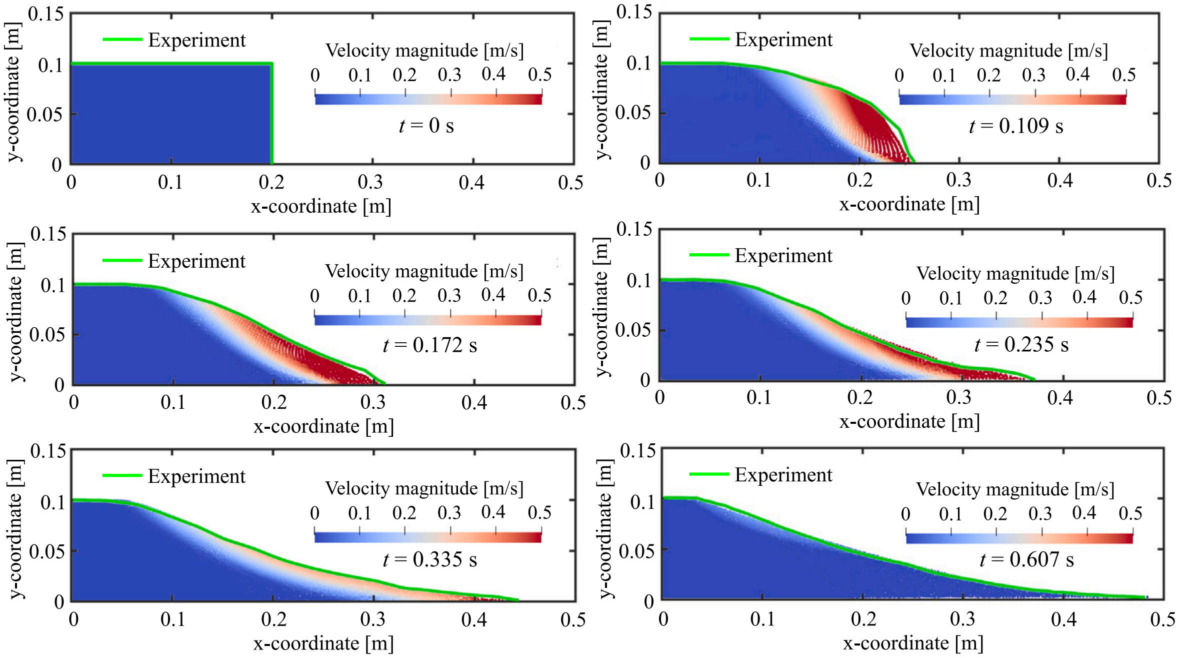

Fig. 15. 2D granular column collapse: comparison of the soil column ($L = 0.2$ m) profiles at different times between SPH simulations and experimental results (Nguyen et al., 2017).

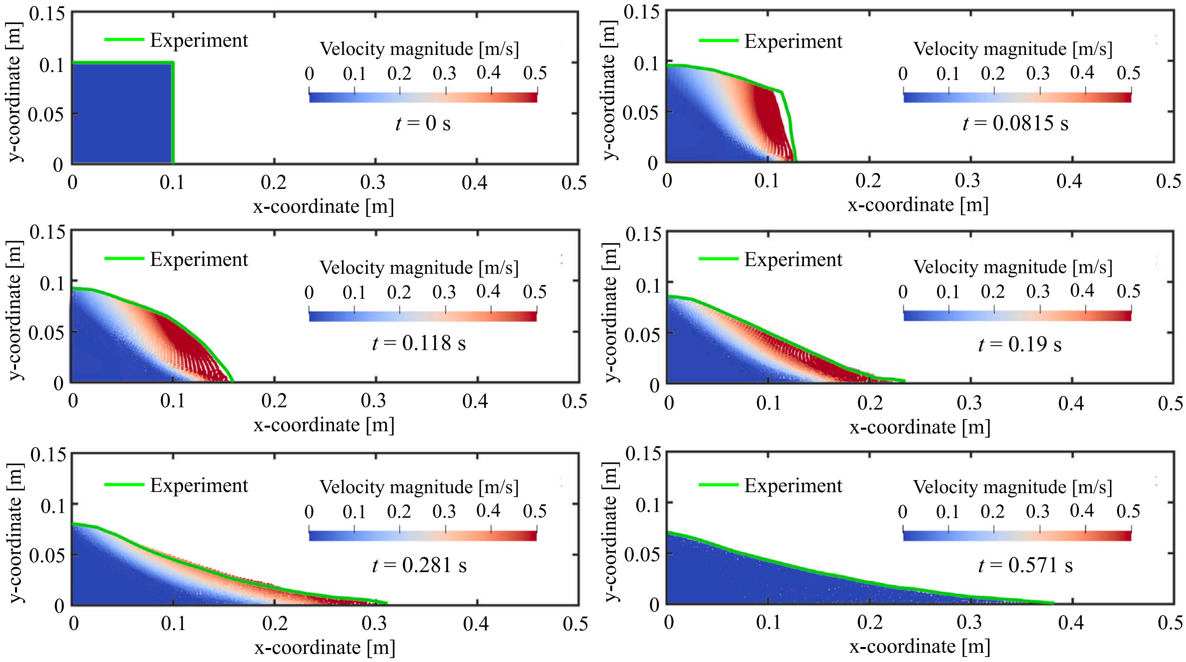

Fig. 16. 2D granular column collapse: comparison of the soil column ($L = 0.1$ m) profiles at different times between SPH simulations and experimental results (Nguyen et al., 2017).

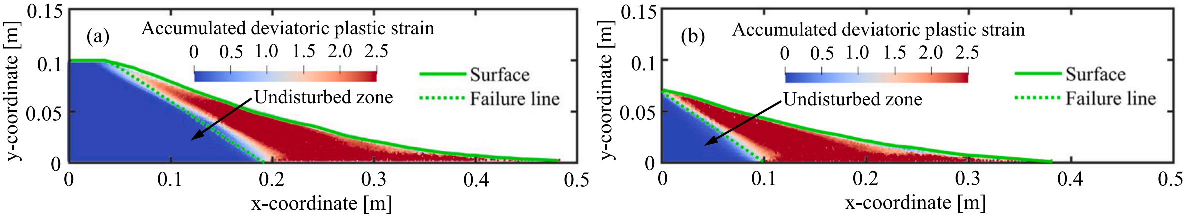

Fig. 17. 2D granular column collapse: illustration of the accumulated deviatoric plastic strain for the final deposit of the column with (a) $L = 0.2$ m and (b) $L = 0.1$ m.

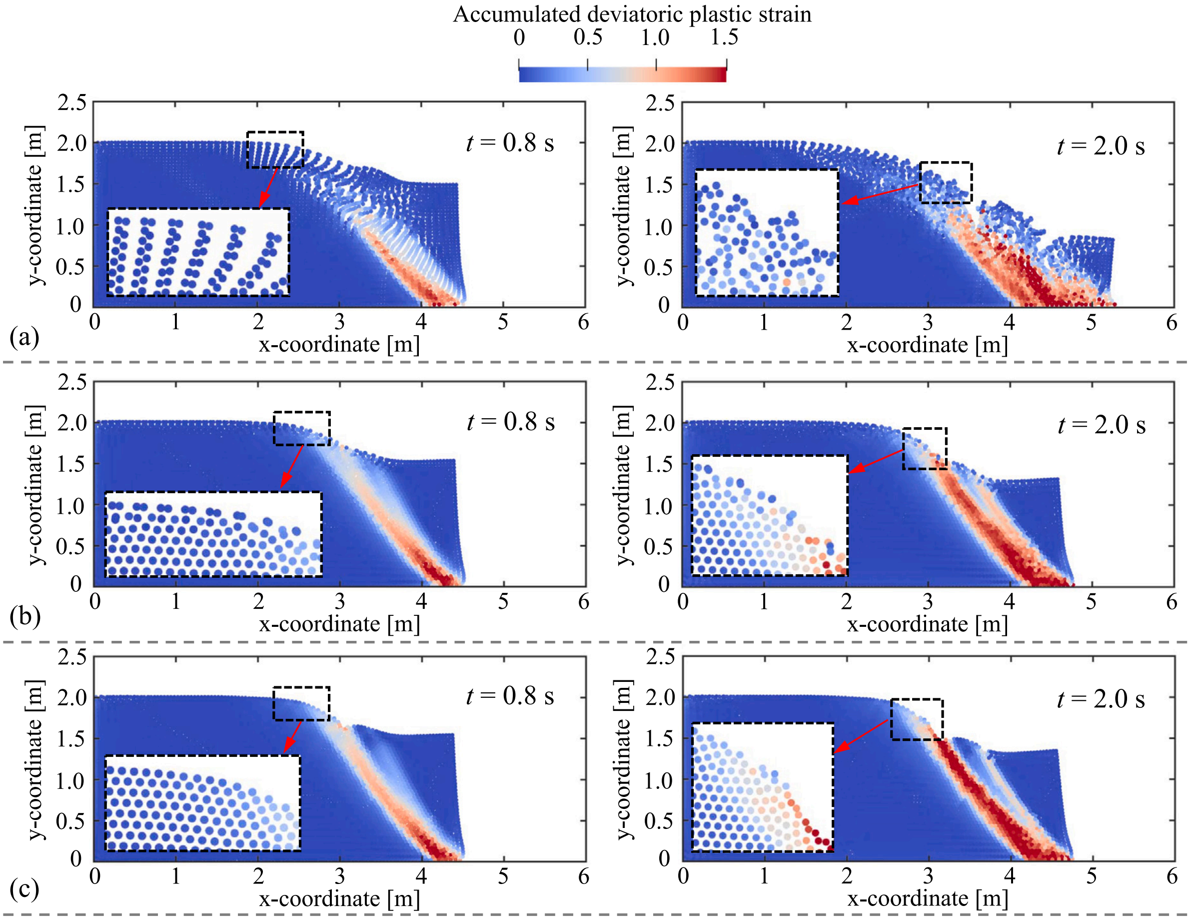

Fig. 18. 2D failure of cohesive granular materials: evolution of particle configuration with time (t = 0.8 s and 2.0 s) for SPH simulations (a) without correction, (b) with TVF, and (c) with UTVF. $dp = L/100$.

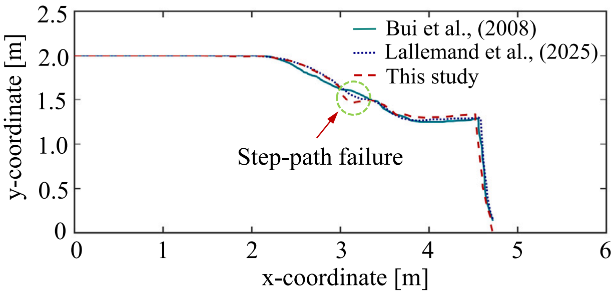

Fig. 19. 2D failure of cohesive granular materials: the contour shape at t = 2.0 s. The results with artificial stress (Bui et al., 2008) and particle shifting (Lallemand et al., 2025) are also shown for comparison. $dp = L/100$.

method inherently has minimal energy dissipation, enabling it to capture the step-path failure phenomenon at a lower resolution, which other methods require higher resolutions to achieve.

Fig. 20 shows the distribution of accumulated deviatoric plastic strain and vertical stress (t = 2 s) obtained using the UTVF correction when the resolution is doubled. As the resolution increases, the step-path failure phenomenon becomes more pronounced, and the shear band changes from a wide, thick single band to several narrow bands. This aligns with the results presented in the literature (Lallemand et al., 2025). Additionally, the vertical stress exhibits a smooth distribution.

Fig. 21 illustrates the final resting state (t = 2 s) of the soil column simulated using the UTVF approach, where the values of cohesion c and friction angle ϕ were varied independently, while other parameters remained constant. These are representative values for soils in Hong Kong (GEO, 2020) and reflect their cohesive, granular nature. It can be observed that as the cohesion and friction angle increase, the shear band gradually shifts to the right, and the undisturbed region on the left side of the shear band expands. The failure mode evolves from retrogressive slips at lower cohesion and friction angle to a single block failure at higher friction angles. Notably, in this case, the increase in cohesion significantly reduces the deformation of the soil column due to the enhanced shear strength, which aligns with our expectations. Regardless of the variations in cohesion and friction angle, a uniform particle distribution is ultimately achieved without exhibiting tensile instability, demonstrating the robustness and general applicability of the proposed method for a wide range of parameter values.

5.3. 3D failure of cohesive granular materials

As mentioned earlier, the extension of the artificial stress method to three dimensions is complex (Bui and Nguyen, 2021; Zhang et al., 2024a). In this section, we will demonstrate that the present UTVF can effectively eliminate tensile instability in 3D scenarios, without

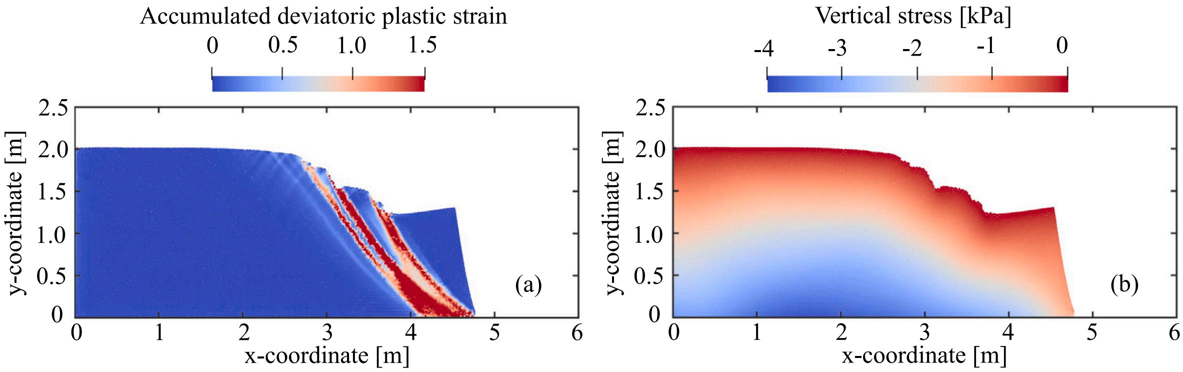

Fig. 20. 2D failure of cohesive granular materials: the distribution of (a) accumulated deviatoric plastic strain and (b) vertical stress at $t = 2.0$ s with $dp = L/200$.

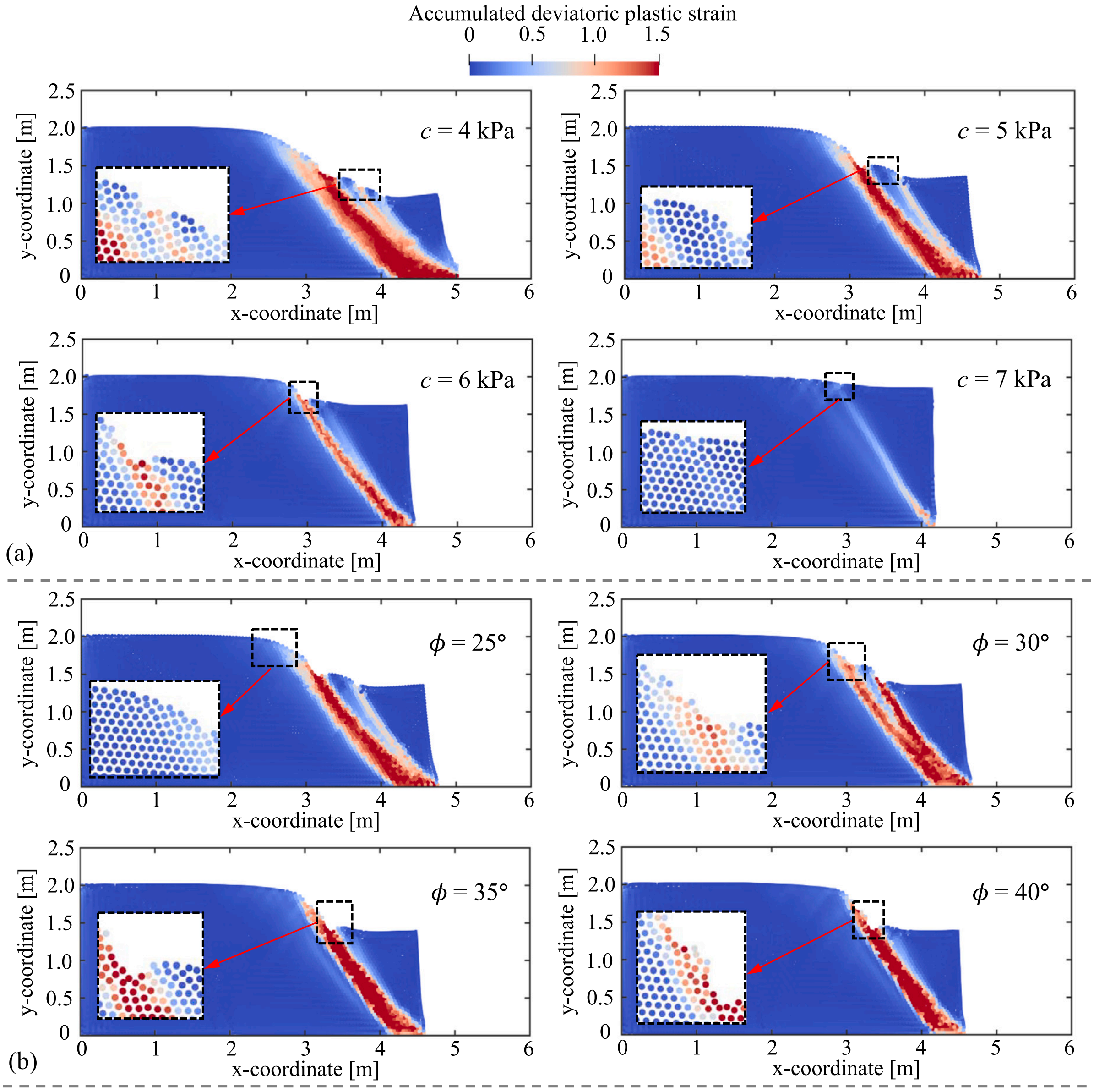

Fig. 21. 2D failure of cohesive granular materials: final states ($t = 2$ s) of the soil column simulated using the UTVF, with variations in (a) cohesion c and (b) friction angles ϕ. Other parameters remain consistent with those listed in Table 2. $dp = L/100$.

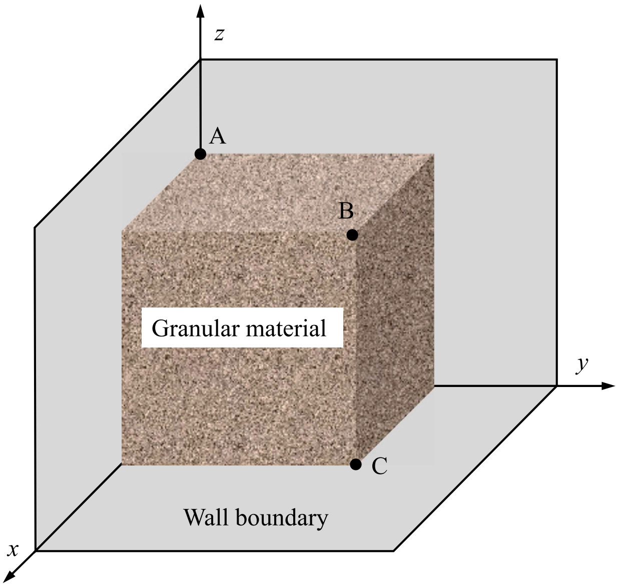

Fig. 22. 3D failure of cohesive granular materials: model setup. The edge length of the cubic soil column is 2 m.

introducing additional complexity compared to the 2D case.

The model setup is shown in Fig. 22, where a cubic soil column with an edge length of 2 m is subjected to self-weight loading. The material parameters are consistent with those in the 2D case, as listed in Table 2. The soil column is discretized with a particle spacing of $dp = 0.04$ m. Fig. 23 shows the particle configuration and velocity distribution at $t = 0.5$ s and $t = 1.0$ s for SPH simulations without correction, with TVF, and with UTVF. Without any correction, severe tensile instability arises in the 3D scenario, leading to pronounced particle clustering and non-physical fractures. The application of TVF improves the regularity of the inner particle distribution; however, tensile instability persists among the free-surface particles. In contrast, the proposed UTVF effectively eliminates tensile instability in the 3D scenario, achieving a uniform distribution of both inner and free-surface particles. Fig. 24 shows the distribution of accumulated deviatoric plastic strain on surface ABC (as shown in Fig. 22) at different times using the present UTVF. The soil column undergoes a failure process, with the shear band gradually propagating from the top to the bottom of the soil column.

5.4. 3D cohesive granular flow

The flow of cohesive granular materials on an inclined flume with a barrier is simulated to demonstrate the capability of the proposed UTVF in preventing tensile instability under significant deformation conditions. The model setup is shown in Fig. 25a, where a rectangular soil mass is placed on the top of the flume. The inclined flume forms an angle of 50 degrees with the horizontal plane. The material parameters are as listed in Table 2.

Fig. 25 presents snapshots of the numerical simulation at various time steps, colored by velocity magnitude. The granular material moves downward under the influence of gravity and eventually comes to rest in front of the barrier. The magnified inset images reveal that tensile instability does not occur throughout the entire process, with the particle distribution remaining uniformly distributed. This indicates that the proposed UTVF is effective in preventing tensile instability even in 3D granular flows.

6. Conclusions

This study extends the TVF, based on local particle consistency, to free surfaces and proposes the UTVF to address tensile instability in large deformation and failure problems of cohesive granular materials under both 2D and 3D scenarios. The developed approach requires only a single coefficient, which is generally applicable across all cases presented in this study, including tests on fluids, elastic materials, and plastic materials.

The UTVF is first validated in simulations of fluids and elastic materials with analytical solutions, demonstrating its convergence, stability, and accuracy. The results also reveal that, compared to particle shifting and optimized particle shifting technique, the UTVF fully conserves linear momentum and exhibits improved angular momentum conservation, while showing significantly reduced energy dissipation compared to dynamic stabilization and artificial stress methods. After validating the Drucker–Prager constitutive model with cohesionless granular materials, the UTVF is applied to simulate the failure of cohesive granular materials in two dimensions, with comparisons made to results obtained using particle shifting and artificial stress methods reported in the literature. Based on the energy dissipation characteristics analyzed in Section 4, the study further explores the reasons for slightly differences in results among the methods. Specifically, the UTVF's minimal dissipation enables it to capture step-path failure phenomena at low resolutions, which other methods require higher resolutions to achieve. Finally, the proposed UTVF is applied to the 3D failure of cohesive granular materials and cohesive granular flows. The results show that, unlike the complex extension of artificial stress to three dimensions, the proposed UTVF can effectively eliminate tensile instability in granular materials in 3D cases without introducing additional computational complexity, thereby enhancing the stability and accuracy of the calculations.

CRediT authorship contribution statement

Shuaihao Zhang: Writing – review & editing, Writing – original draft, Visualization, Validation, Methodology, Investigation, Formal analysis, Conceptualization. **Feng Wang:** Writing – review & editing, Methodology, Investigation. **Xiangyu Hu:** Writing – review & editing, Methodology. **Sérgio D.N. Lourenço:** Writing – review & editing, Supervision, Methodology, Investigation.

Declaration of competing interest

The authors declare that they have no known competing financial interests or personal relationships that could have appeared to influence the work reported in this paper.

Acknowledgments

Sérgio D.N. Lourenço would like to express his gratitude to the Research Grants Council Hong Kong for their sponsorship of this research under a Collaborative Research Fund (C6006-20GF). The computations were performed using research computing facilities offered by Information Technology Services, the University of Hong Kong.

Data availability

Data will be made available on request.

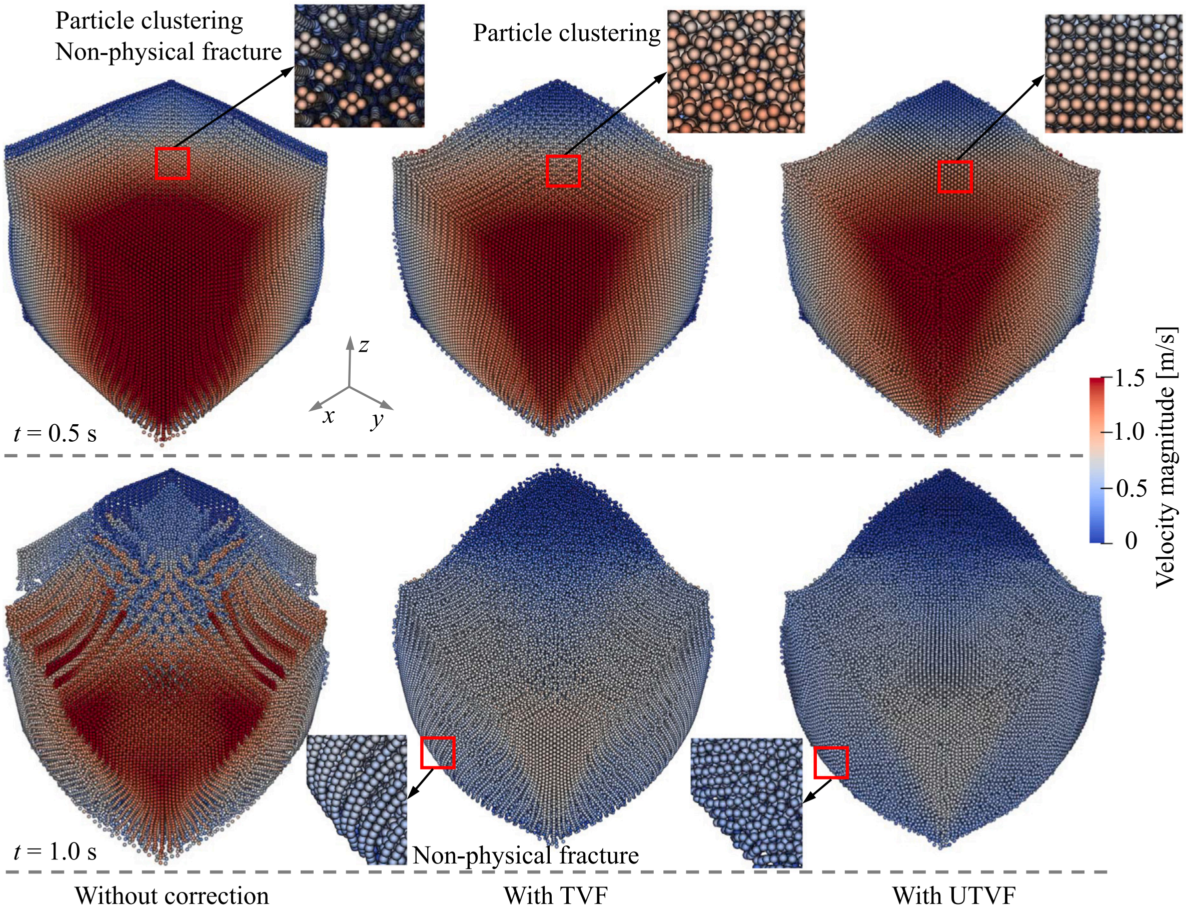

Fig. 23. 3D failure of cohesive granular materials: evolution of particle configuration with time ($t = 0.5$ s and 1.0 s) for SPH simulations without correction, with TVF, and with UTVF, respectively. The particles are colored by velocity magnitude and $dp = 0.04$ m.

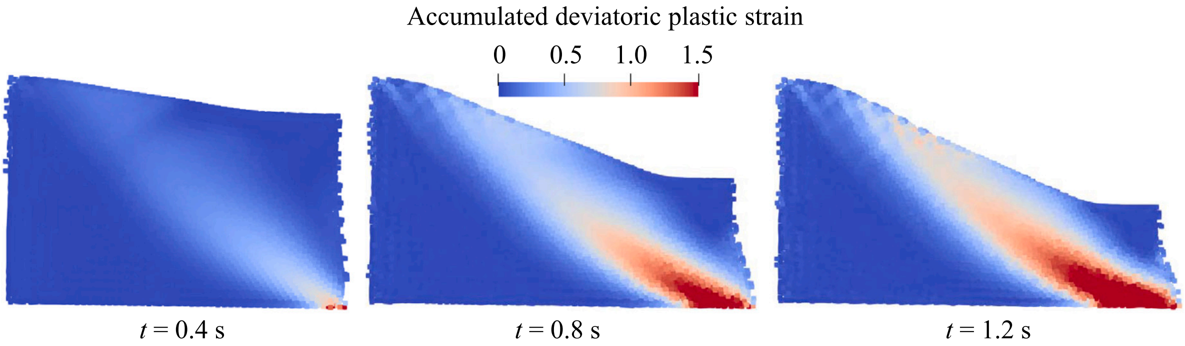

Fig. 24. 3D failure of cohesive granular materials: the distribution of accumulated deviatoric plastic strain on surface ABC at different times with the present UTVF. $dp = 0.04$ m.

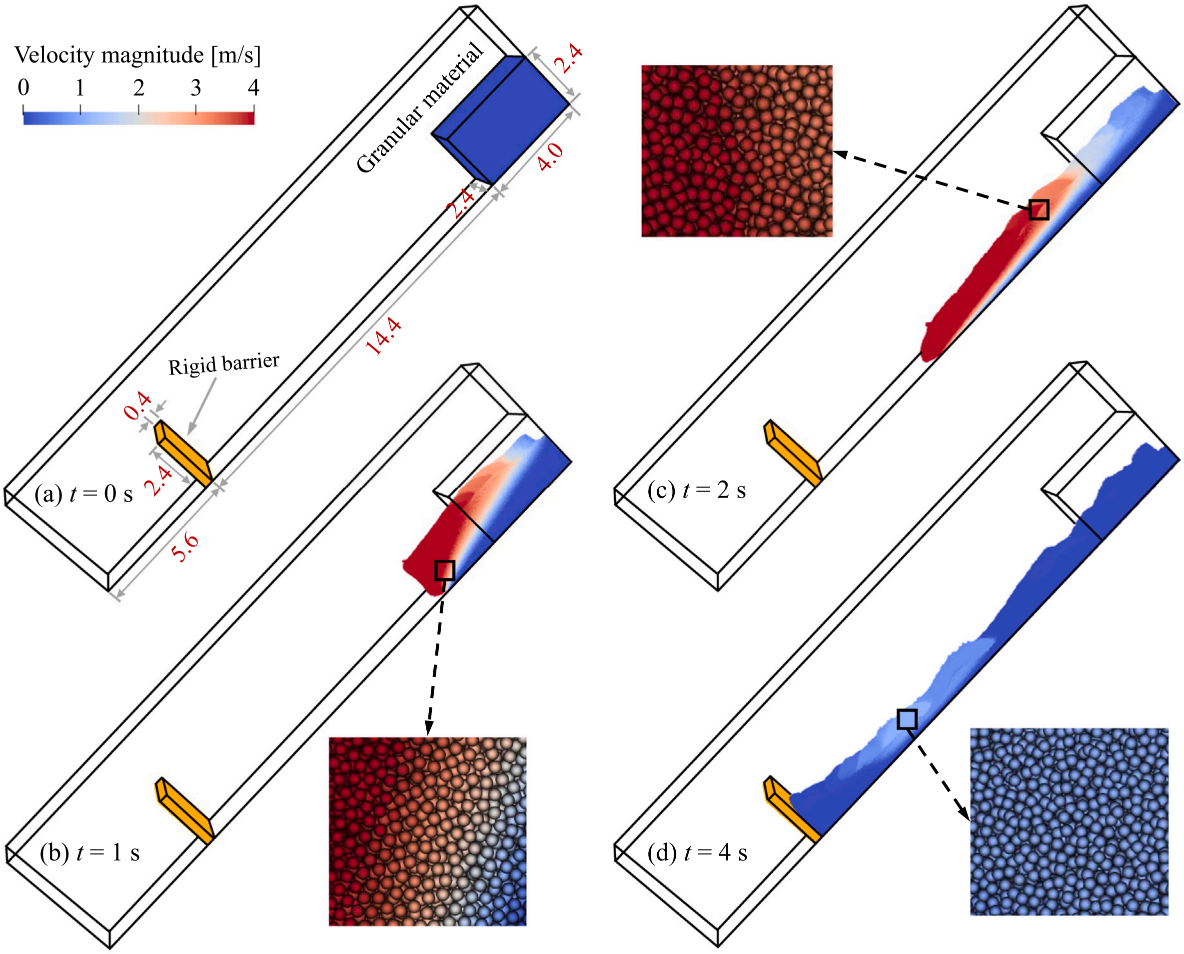

Fig. 25. 3D cohesive granular flow: snapshots of granular flows on an inclined flume at different times ($t = 0$ s, 1 s, 2 s and 4 s). The particles are colored by velocity magnitude and $dp = 0.04$ m. The units of the values in subplot (a) are all in meters.

References

Adami, S., Hu, X., Adams, N.A., 2013. A transport-velocity formulation for smoothed particle hydrodynamics. J. Comput. Phys. 241, 292–307.

Borja, R.I., 2013. Plasticity, vol. 10, Springer Berlin Heidelberg, 59–115.

Borja, R.I., Tamagnini, C., 1998. Cam-Clay plasticity Part III: Extension of the infinitesimal model to include finite strains. Comput. Methods Appl. Mech. Engrg. 155 (1–2), 73–95.

Brackbill, J.U., Kothe, D.B., Zemach, C., 1992. A continuum method for modeling surface tension. J. Comput. Phys. 100 (2), 335–354.

Bui, H.H., Fukagawa, R., Sako, K., Ohno, S., 2008. Lagrangian meshfree particles method (SPH) for large deformation and failure flows of geomaterial using elastic–plastic soil constitutive model. Int. J. Numer. Anal. Methods Geomech. 32 (12), 1537–1570.

Bui, H.H., Nguyen, G.D., 2021. Smoothed particle hydrodynamics (SPH) and its applications in geomechanics: From solid fracture to granular behaviour and multiphase flows in porous media. Comput. Geotech. 138, 104315.

Chen, W., Mizuno, E., 1990. Nonlinear Analysisin Soil Mechanics-Theory and Implementation. Elsevier Science Publishers BV, Amsterdam.

Colagrossi, A., 2005. A Meshless Lagrangian Method for Free-Surface and Interface Flows with Fragmentation (These). Universita di Roma.

del Castillo, E.M., Fávero Neto, A.H., Geng, J., Borja, R.I., 2024. An SPH framework for drained and undrained loading over large deformations. Int. J. Numer. Anal. Methods Geomech..

Dienes, J.K., 1979. On the analysis of rotation and stress rate in deforming bodies. Acta Mech. 32 (4), 217–232.

Drucker, D.C., Prager, W., 1952. Soil mechanics and plastic analysis or limit design. Quart. Appl. Math. 10 (2), 157–165.

Espanol, P., Revenga, M., 2003. Smoothed dissipative particle dynamics. Phys. Rev. E 67 (2), 026705.

Feng, R., Fourtakas, G., Rogers, B.D., Lombardi, D., 2021. Large deformation analysis of granular materials with stabilized and noise-free stress treatment in smoothed particle hydrodynamics (SPH). Comput. Geotech. 138, 104356.

Feng, R., Fourtakas, G., Rogers, B.D., Lombardi, D., 2022. Two-phase fully-coupled smoothed particle hydrodynamics (SPH) model for unsaturated soils and its application to rainfall-induced slope collapse. Comput. Geotech. 151, 104964.

GEO, 2020. Guide to Retaining Wall Design (Geoguide 1). Geotechnical Engineering Office, Civil Engineering and Development Department, HKSAR Government, Hong Kong, p. 245.

Gingold, R.A., Monaghan, J.J., 1977. Smoothed particle hydrodynamics: theory and application to non-spherical stars. Mon. Not. R. Astron. Soc. 181 (3), 375–389.

Gray, J.P., Monaghan, J.J., Swift, R., 2001. SPH elastic dynamics. Comput. Methods Appl. Mech. Engrg. 190 (49–50), 6641–6662.

Hoang, T.N., Nguyen, T.T., Nguyen, T.V., Nguyen, G.D., Bui, H.H., 2024. SPH simulation of earthquake-induced liquefaction and large deformation behaviour of granular materials using SANISAND constitutive model. Comput. Geotech. 174, 106617.

Hu, X.Y., Adams, N.A., 2006. A multi-phase SPH method for macroscopic and mesoscopic flows. J. Comput. Phys. 213 (2), 844–861.

Hurley, R.C., Andrade, J.E., 2017. Continuum modeling of rate-dependent granular flows in SPH. Comput. Part. Mech. 4, 119–130.

Jop, P., Forterre, Y., Pouliquen, O., 2006. A constitutive law for dense granular flows. Nature 441 (7094), 727–730.

Khayyer, A., Gotoh, H., Shimizu, Y., 2017. Comparative study on accuracy and conservation properties of two particle regularization schemes and proposal of an optimized particle shifting scheme in ISPH context. J. Comput. Phys. 332, 236–256.

Lallemand, M., De Sousa, C., Hermange, C., Michel, J., Oger, G., 2025. A Riemann-based SPH formulation for modelling elastoplastic soil behaviour using a Drucker–Prager model. J. Terramechanics 117, 101033.

Landau, L.D., Lifshitz, E.M., 2013. Course of Theoretical Physics. Elsevier.

Le Touzé, D., Colagrossi, A., Colicchio, G., Greco, M., 2013. A critical investigation of smoothed particle hydrodynamics applied to problems with free-surfaces. Internat. J. Numer. Methods Fluids 73 (7), 660–691.

Lee, E.S., Moulinec, C., Xu, R., Violeau, D., Laurence, D., Stansby, P., 2008. Comparisons of weakly compressible and truly incompressible algorithms for the SPH mesh free particle method. J. Comput. Phys. 227 (18), 8417–8436.

Lemiale, V., Mühlhaus, H.-B., Meriaux, C., Moresi, L., Hodkinson, L., 2011. Rate effects in dense granular materials: Linear stability analysis and the fall of granular columns. Int. J. Numer. Anal. Methods Geomech. 35 (2), 293–308.

Lian, Y., Bui, H.H., Nguyen, G.D., Zhao, S., Haque, A., 2022. A computationally efficient SPH framework for unsaturated soils and its application to predicting the entire rainfall-induced slope failure process. Géotechnique 1–19.

Lind, S.J., Xu, R., Stansby, P.K., Rogers, B.D., 2012. Incompressible smoothed particle hydrodynamics for free-surface flows: A generalised diffusion-based algorithm for stability and validations for impulsive flows and propagating waves. J. Comput. Phys. 231 (4), 1499–1523.

Lucy, L.B., 1977. A numerical approach to the testing of the fission hypothesis. Astron. J. 82, 1013–1024.

Madraki, Y., Hormozi, S., Ovarlez, G., Guazzelli, E., Pouliquen, O., 2017. Enhancing shear thickening. Phys. Rev. Fluids 2 (3), 033301.

Monaghan, J.J., 1994. Simulating free surface flows with SPH. J. Comput. Phys. 110 (2), 399–406.

Monaghan, J.J., 2000. SPH without a tensile instability. J. Comput. Phys. 159 (2), 290–311.

Morris, J.P., Fox, P.J., Zhu, Y., 1997. Modeling low Reynolds number incompressible flows using SPH. J. Comput. Phys. 136 (1), 214–226.

Nguyen, C.T., Nguyen, C.T., Bui, H.H., Nguyen, G.D., Fukagawa, R., 2017. A new SPH-based approach to simulation of granular flows using viscous damping and stress regularisation. Landslides 14, 69–81.

Oger, G., Doring, M., Alessandrini, B., Ferrant, P., 2007. An improved SPH method: Towards higher order convergence. J. Comput. Phys. 225 (2), 1472–1492.

Peng, C., Xu, G., Wu, W., Yu, H.s., Wang, C., 2017. Multiphase SPH modeling of free surface flow in porous media with variable porosity. Comput. Geotech. 81, 239–248.

Randles, P., Libersky, L.D., 1996. Smoothed particle hydrodynamics: some recent improvements and applications. Comput. Methods Appl. Mech. Engrg. 139 (1–4), 375–408.

Ren, Y., Lin, P., Zhang, C., Hu, X., 2023. An efficient correction method in Riemann SPH for the simulation of general free surface flows. Comput. Methods Appl. Mech. Engrg. 417, 116460.

Simo, J.C., Hughes, T.J., 2006. Computational Inelasticity, vol. 7, Springer Science & Business Media.

Swegle, J.W., Hicks, D.L., Attaway, S.W., 1995. Smoothed particle hydrodynamics stability analysis. J. Comput. Phys. 116 (1), 123–134.

Tsuruta, N., Khayyer, A., Gotoh, H., 2013. A short note on dynamic stabilization of moving particle semi-implicit method. Comput. & Fluids 82, 158–164.

Wang, Z., Haidn, O.J., Hu, X., 2024. The efficient implementation of transport velocity formulation. arXiv preprint arXiv:2411.13992.

Wendland, H., 1995. Piecewise polynomial, positive definite and compactly supported radial functions of minimal degree. Adv. Comput. Math. 4, 389–396.

Xu, R., Stansby, P., Laurence, D., 2009. Accuracy and stability in incompressible SPH (ISPH) based on the projection method and a new approach. J. Comput. Phys. 228 (18), 6703–6725.

Yang, E., Bui, H.H., Nguyen, G.D., Choi, C.E., Ng, C.W., De Sterck, H., Bouazza, A., 2021. Numerical investigation of the mechanism of granular flow impact on rigid control structures. Acta Geotech. 16, 2505–2527.

Zhan, L., Peng, C., Zhang, B., Wu, W., 2019. Three-dimensional modeling of granular flow impact on rigid and deformable structures. Comput. Geotech. 112, 257–271.

Zhang, B., Adams, N., Hu, X., 2025a. Towards high-order consistency and convergence of conservative SPH approximations. Comput. Methods Appl. Mech. Engrg. 433, 117484.

Zhang, C., Hu, X.Y., Adams, N.A., 2017a. A generalized transport-velocity formulation for smoothed particle hydrodynamics. J. Comput. Phys. 337, 216–232.

Zhang, C., Hu, X., Adams, N.A., 2017b. A weakly compressible SPH method based on a low-dissipation Riemann solver. J. Comput. Phys. 335, 605–620.

Zhang, S., Lourenço, S.D., Wu, D., Zhang, C., Hu, X., 2024a. Essentially non-hourglass SPH elastic dynamics. J. Comput. Phys. 113072.

Zhang, C., Rezavand, M., Hu, X., 2021a. A multi-resolution SPH method for fluid-structure interactions. J. Comput. Phys. 429, 110028.

Zhang, C., Rezavand, M., Zhu, Y., Yu, Y., Wu, D., Zhang, W., Wang, J., Hu, X., 2021b. SPHinXsys: An open-source multi-physics and multi-resolution library based on smoothed particle hydrodynamics. Comput. Phys. Comm. 267, 108066.

Zhang, S., Wu, D., Hu, X., Choi, C.E., Lourenço, S.D., 2025b. An efficient SPH framework for modelling binary granular mixtures and implications for granular flows. Int. J. Numer. Anal. Methods Geomech. 49 (3), 815–838.

Zhang, S., Wu, D., Lourenço, S.D., Hu, X., 2024b. A generalized non-hourglass updated Lagrangian formulation for sph solid dynamics. arXiv preprint arXiv:2409.11474.

Zhang, S., Zhang, C., Hu, X., Lourenço, S.D., 2024c. A Riemann-based SPH method for modelling large deformation of granular materials. Comput. Geotech. 167, 106052.

Zhang, S., Zhang, W., Zhang, C., Hu, X., 2023. A Lagrangian free-stream boundary condition for weakly compressible smoothed particle hydrodynamics. J. Comput. Phys. 490, 112303.

Zhu, C., Peng, C., Wu, W., 2022. Lagrangian meshfree particle method (SPH) based simulation for granular flow in a rotating drum with regularized μ (I) elastoplastic model. Powder Technol. 408, 117699.

Zhu, Y., Zhang, C., Hu, X., 2021. A consistency-driven particle-advection formulation for weakly-compressible smoothed particle hydrodynamics. Comput. & Fluids 230, 105140.